

Axon Initial Segment Pathology in Alzheimer's Disease Mouse Model Disturbs the Action Potential Initiation and Propagation

Zhiya Chen

Peking University

Luxin Peng

Peking University

Mengdi Zhao

Peking University

Louis Tao

Peking University

Peng Zou

Peking University

Yan Zhang (✉ yanzhang@pku.edu.cn)

Peking University School of Life Sciences

Research Article

Keywords: Alzheimer's disease, Action potential, Axon initial segment, Velocity, Propagation

Posted Date: October 20th, 2021

DOI: <https://doi.org/10.21203/rs.3.rs-929763/v1>

License: © ⓘ This work is licensed under a Creative Commons Attribution 4.0 International License.

[Read Full License](#)

Abstract

Axonal pathology has been widely reported in Alzheimer's disease (AD). As a highly structured region in the axon, axon initial segment (AIS) plays a vital role in action potential (AP) dynamics, including initiation and propagation, closely linked to neuronal excitability and neurotransmitter release kinetics. Previously, we showed that proteins localized in the AIS were remarkably changed in neurons from APP_{swe}/PS1_{ΔE9} mice carrying familial AD mutations. However, whether the AIS defects in APP/PS1 mouse neurons affect AP dynamics is unknown. Using genetically-encoded voltage indicators (GEVIs)-based voltage imaging, we studied AP initiation and propagation in the APP/PS1 neurons. We found that APP/PS1 neurons were more sensitive to intensive stimulations. Our data suggested that AP velocities significantly decreased in neurons from APP/PS1 mice than the wild-type mice. The velocity of forward-propagating action potentials was lower when the AIS was located more distally from the soma or when the AIS had a shorter length. The velocity of back-propagating action potentials was not correlated with the location nor with the length of the AIS. These experimental results were reproduced in neuronal simulations using multi-compartment modeling, suggesting a correlation between AIS length/location change and AP propagation velocity due to the distribution of sodium channels. Taken together, Our findings provide a deep insight into the abnormality of neuronal function in AD.

Introduction

Alzheimer's disease (AD) is a severe neurodegenerative disorder characterized by progressive age-dependent degeneration of neurons in the central nervous system and representing the most common type of dementia in the elderly [1]. The brains of AD patients are characterized by numerous extracellular senile plaques composed of amyloid β (A β), intracellular tau aggregates, and neuronal loss [2]. Previous studies indicated that AD was typically associated with cytoskeletal alterations, including the formation of neurofibrillary tangles (NFTs), neuropil threads, and axonal pathology [3-8]. Our previous study showed that in the hippocampal neurons from typical AD model APP_{swe}/PS1_{ΔE9} mice, proteins enriched in the axon initial segment (AIS), such as ankyrin G (AnkG) and neurofascin 186 (NF186), were remarkably down-regulated [9]. Moreover, AnkG-deficiency impaired the proper localization of Na_{v1.6} channels in the AIS and generated dispersive Na_{v1.6} channels distribution in the entire axon [9].

The AIS is a highly structured region consisting of scaffolding proteins, adaptor protein (e.g., AnkG), transmembrane cell adhesion molecules (e.g., NF186), and a dense population of voltage-gated ion channels (e.g., Na_{v1.2} and Na_{v1.6}) [10-12]. It plays a vital role in brain diseases and injuries [13]. APs are generated at the AIS and propagated in two directions, i.e., forward-propagating action potentials (fpAPs) and back-propagating action potentials (bpAPs) [14-16]. fpAPs travel along the axon toward the axonal terminal and trigger the neurotransmitter release onto the adjacent target cells. Whereas, bpAPs travel toward the soma and the dendrites [17, 18]. The relationship between bpAPs and the input electrical signals in the dendrites is associated with the induction and maintenance of long-term potentiation (LTP) or long-term depression (LTD), vital to the long-lasting increase or decrease of the connection between

neurons [19-22]. During these processes, the velocity of AP propagation significantly influences the timing of electrical signaling, which is key to information transformation and integration. AP propagation velocity varies in response to physiological fluctuations [23-28]. However, whether the AIS pathology affects the AP initiation and propagation is unknown.

To measure AP propagation velocity, a multi-site simultaneous recording is needed. However, due to the tiny structure of the axonal structure (less than 1 μm in diameter), the classical patch-clamp technique is not readily applicable to the axon [29]. One possible approach is to create an “axonal bleb” in the brain slices. [29-31]. However, the multi-site recording in the axon and the AIS via patch-clamp is nearly impossible [26, 30]. The other solution is using a high-density microelectrode array (HD-MEA) to measure the AP propagation in the AIS with high temporal resolution [32-35]. While these electrode-based techniques have advanced our knowledge of AIS electrophysiological properties, they suffer from high invasiveness to cells, lower spatial sampling density, poor spatial resolution, and increased costs. In recent years, voltage imaging has emerged as a powerful tool to report AP with high spatial-temporal resolution and high throughput in sub-compartments of the axon, such as the AIS [33, 36-39]. With the development of genetically encoded voltage indicators (GEVIs), voltage imaging can provide more spatial information on AP waveforms in the AIS and are cost-effective than HD-MEA methods. It has been used in studying AP initiation and propagation manners in the tiny and fragile AIS in the past decades [40-43].

Herein, using GEVIs-based voltage imaging, we studied AP initiation and propagation dynamics in the AIS of cultured mouse hippocampal neurons. We reported that compared with the neurons from wild-type mice, the AP initiation site of the neurons from APP/PS1 mice was significantly far away from the soma, and AP velocities in their AIS were lower. Besides, in wild-type neurons, the fpAP velocity was negatively correlated with the AIS-to-soma distance but was positively correlated with the AIS length. Taken together, our results elucidated the abnormal intrinsic excitability, AP initiation site, and bidirectional propagation patterns in the APP/PS1 neurons, which may be induced by AD axonal pathology and contribute to AD pathology.

Methods

Reagents, Plasmids, and Antibodies

Poly-D-Lysine (PDL), Tween-20, Triton-100, Hanks' balanced salt solution (HBSS), Bovine Serum Albumin (BSA), fetal bovine serum, and fetal calf serum were from Sigma. DMEM medium, Neurobasal medium, GlutaMAX, B27 supplement, penicillin/streptomycin, and trypsin were from Gibco. Tyrode's Salts solution was from Macgene. The anti-Neurofascin antibody (extNF; A12/18) was from NeuroMab. The anti-ankyrin G antibody was from Invitrogen. The anti-MAP2 antibody was from Abcam. Alexa Fluor[®] 405 Goat Anti-Mouse, Alexa Fluor[®] 488 Donkey Anti-Mouse, and Alexa Fluor[®] 568 Donkey Anti-Chicken were from Invitrogen.

Animals

SD rats, C57BL/6J mice, and APP/PS1 (APP_{SWE}/PS1_{ΔE9}; human APP Swedish mutant/human PS1 exon 9 deletion) mice were from Beijing Vital River Laboratory Animal Technology Co., Ltd., following the rules and regulations of Peking University Animal Care and Use Committee as described previously [9, 44].

Dissociation of Hippocampal Cultures

According to standard protocols, we prepared dissociated mixed neuronal and glial cultures from postnatal day 0 rat/mouse pups hippocampi. Briefly, hippocampi were dissected in DMEM, digested in 0.25% trypsin (15 min 37°C), triturated through Pasteur pipettes of increasingly narrow diameter, and plated at 60,000 cells mL⁻¹ onto PDL (50 μg mL⁻¹) coated glass-bottom dishes (Cellvis). Cultures were incubated (37°C, 5% CO₂) in the Neurobasal medium containing B27 supplement, 2 mM GlutaMAX, and penicillin/streptomycin. The medium was half-replaced after 48 hours.

Transfection

Calcium phosphate transfection was used to introduce QuasAr2-mOrange2 plasmid directly into the cell at days 8 *in vitro* (DIV7). Generally, for every dish, 2 μg of QuasAr2 plasmid in a 12.4 μL CaCl₂/water solution was mixed with 2× HEPES balanced solution (pH 7.12) followed by gentle vortexing. The plasmid–Ca²⁺–phosphate complex was formed after 10 min incubation at room temperature and then dropwisely added to DIV6 neurons prewashed with Neurobasal medium on glass-bottom dishes. Cultures were incubated in a humidified 5% CO₂ chamber at 37°C for 30 min, and precipitation could be observed around the cells. The precipitation was dissolved by adjusting the medium pH to 6.8 and 5 min incubation at 37°C. Finally, cells were fed with the original growth medium and maintained until DIV12 for live imaging, immunofluorescence, or other treatment as described below.

ALS live-labeling

The mouse anti-pan-neurofascin antibody (extNF; A12/18, Neuromab) was generated against the rat-specific extracellular domain common to NF155 and NF186 (amino acids 25-1110). Cultured neurons at DIV12 were washed three times in HBSS, transferred into primary antibody solution (1:200), and incubated in a humidified 5% CO₂ chamber at 37°C for another 30 min. Next, cultures were washed three times in HBSS, transferred in secondary antibody (anti-mouse 405, 1:500), and incubated in a humidified 5% CO₂ chamber at 37°C for another 30 min. Finally, the cultures were rewashed and transferred into Tyrodé's buffer (MACGENE) for imaging.

Immunocytochemistry

Following primary antibodies were used: mouse anti-ankyrin G (1:500; Invitrogen), chicken anti-MAP2 (1:10000; Abcam). Cultures were fixed with 4% paraformaldehyde and incubated with primary antibody for 1 hour at room temperature. After washed in Tyrode's buffer, permeabilized in 0.2% Triton X-100 (Sigma; 5 min at room temperature), and blocked in 5% BSA (Sigma; 1 hour at room temperature), cultures were transferred in the medium containing primary antibody solution (in 5% BSA). The cultures were then washed three times and transferred into the medium containing dye-conjugated secondary antibodies mentioned before for 1 hour at room temperature. Then the cultures were washed three times and transferred into Tyrode's buffer for imaging.

Imaging apparatus

Fluorescence imaging experiments were conducted on an inverted fluorescence microscope (Nikon-TiE) equipped with a 40X 1.3 NA oil immersion objective lens, six laser lines (Coherent OBIS, 405 nm, 488 nm, 532 nm, 561 nm, 637 nm for confocal imaging, and a high-intensity 637 nm for voltage imaging), a spinning disk confocal unit (Yokogawa CSU-X1), and two scientific CMOS cameras (Hamamatsu ORCA-Flash 4.0 v2). The microscope, lasers, and the camera were controlled with a customized software written in LabVIEW (National Instruments, 15.0 version) and could switch between confocal and widefield imaging modes. Imaging of dyes and fluorescent proteins was performed at illumination intensities of 1–6 W/cm², and imaging of QuasAr2 was performed at 900 W/cm². Supplementary Table S1 summarizes the laser lines, dichroic mirrors, and emission filters used for fluorescence imaging.

Confocal imaging of neurons

After labeling, cultures were transferred to Tyrode's buffer (MACGENE). Images were acquired at 1×1 camera binning with an exposure time of 100-1000 milliseconds in Z-stack mode with a 0.3-0.5 μm step length. Each image stack would be with Z-axis max intensity projection, and the new projected images in several channels would be adjusted and merged with ImageJ/Fiji (NIH)

Simultaneous patch-clamp recording and fluorescence imaging

Cultured hippocampal neurons from rats/mice were cultured, transfected, and labeled as described above. All imaging and electrophysiology experiments were performed in a customized high-glucose Tyrode's buffer containing 125 mM NaCl, 2.5 mM KCl, 3 mM CaCl₂, 1 mM MgCl₂, 10 mM HEPES, 30 mM glucose (pH 7.3) and adjusted to 305–310 mOsm/kg with sucrose. The synapse blockers D-APV (25 μM), NBQX (10 μM), and Gabazine (20 μM) (all from Abcam) were added to the imaging medium for single-cell measurement.

We performed electrophysiology experiments at room temperature. Borosilicate glass electrodes (Sutter) were pulled to a tip resistance of 2.5-5 M Ω , and Recordings were terminated if membrane resistance changed by > 10%. The glass electrode was filled with internal solution containing 125 mM potassium gluconate, 8 mM NaCl, 0.6 mM MgCl₂, 0.1 mM CaCl₂, 1 mM EGTA, 10 mM HEPES, 4 mM Mg-ATP, 0.4 mM Na-GTP (pH 7.3) and adjusted to 295 mOsm/kg with 1M sucrose. A Sutter MP285 micromanipulator was recruited for adjusting the glass electrode's position. The cells were clamped using an Axopatch 200B amplifier (Axon Instruments). The membrane voltage signal recorded from the patch amplifier was filtered with an internal 5 kHz Bessel filter and digitized at 21159.48 Hz (for Fig. 1) or 9681.48 Hz (for other figures) with a National Instruments PCIe-6353 data acquisition (DAQ) board (approximate twice the bandwidth of the Bessel filter).

To collect the spike-triggered average movie from neurons expressing QuasAr2-mOrange2, we clamped the cultured neurons in the whole-cell current-clamp mode (Axopatch 200B, Axon Instruments). We simulated neurons 80 times or 125 times with 10 ms 100 pA-500 pA current injection (the stimulation frequency is 6 Hz or 4 Hz, respectively) and simultaneously recorded the QuasAr2 fluorescence movies of the clamped neuron. The movies were acquired at 484 Hz (2.0658 ms exposure time for each frame) or 1058 Hz frame rate (0.9452 ms exposure time for each frame) in rolling-shutter mode with 2-by-2 binning, and the movies were averaged over all simulated APs (by peak finding and alignment) to boost the signal-to-noise (SNR) ratio for following interpolation and calculation. Camera bias (intensity of 400 in the 2 x 2 binning mode) was subtracted from these average intensities to give the final values. We used QuasAr2 imaging intensity of 900 W/cm² at 637 nm and mOrange2 imaging intensity of 1.0 W/cm² at 532 nm. Signal-to-noise ratio (SNR) The SNR was defined as the ratio of maximum fluorescence change over the standard deviation of baseline fluorescence fluctuations. For all experiments, the fluorescence signal was corrected for the photobleaching effect. The photobleaching baseline was constructed from the whole field intensity by a sliding minimum filter related to the stimulation frequency, followed by a smooth processing algorithm. Then each frame of the raw movie (after camera bias subtraction) was divided by the photobleaching baseline.

Data analysis

The aim of data processing was to calculate the velocity on axons through this periodic signal. The video data were processed by the self-developed method with MATLAB (version R2017a).

The flow chart of the method is shown in Supplementary Fig. S3A. Firstly, the raw data were filtered by a Gaussian low-pass filter (size: 3 x 3, sigma: 1) to remove the spatial noise. As shown in Supplementary Fig. S3B and Supplementary Fig. S3C, spatial filtering increased the contrast of the standard deviation image. The pixels with low standard derivatives were background pixels, while those with large standard deviations were ROI pixels. Spatial filtering reduced the signals of background pixels and the background noise. Next, as shown in Supplementary Fig. S3D, the user would draw the centerline of the axon (the red line). According to the centerline, we set the 5x5 region (the white square) centered by each pixel on the

centerline as the whole region of interest (ROI, the region circled by the white line). Then, we smoothed the intensity of the whole ROI twice to get the photobleaching baseline (Supplementary Fig. S3E). The first smooth was a minimum filtering (window size: 4 x 80), the result was the red line, and the second was mean filtering (window size: 2 x 80); the result was the yellow line, which was the photobleaching baseline. The final normalized signal value was the intensity divided by the photobleaching baseline (Supplementary Fig. S3E lower). After that, we found the peaks (local maximum) of periodic APs (Supplementary Fig. S3F upper) and averaged them to get the mean action potential (blue AP in Supplementary Fig. S3F lower). To increase the time resolution, we interpolated the kernel with a cubic spline to get the green AP used as a kernel to revise the APs on each segment. The cubic spline interpolation made the time resolution of data increased from 2 ms to 0.002 ms.

We then calculated the arrival time of the peak of an action potential on each segment. Each segment was defined by 21 pixels on the centerline. As shown in Supplementary Fig. S3G, the green region was one of the segments. We averaged the signals of pixels in this region to be the signal on the red point, which was the center of the green region. The green region was a small window sliding on the centerline. We first interpolated the signal of the red point (blue signal) with cubic spline as the interpolation on the kernel. Then we convolved the splined signal on the red point (red signal) with the kernel (green signal in Supplementary Fig. S3F) to calculate the correlation coefficient (yellow line in Supplementary Fig. S3G). Then we replaced the splined signal with the kernel according to the correlation coefficient and got the corrected signal (purple signal). After that, we used the corrected and high-precision signal to find the red point's AP peak arrival time. After the green window slides over all pixels on the centerline, we got the corrected APs and their peak arrival time on all locations of the axon (Supplementary Fig. S3H).

Finally, we calculated two types of velocity: the mean velocity and the instantaneous velocity. For mean velocity, we fitted the points in Supplementary Fig. S3H (lower right) with a line linearly. The mean velocity was the slope of the line (Supplementary Fig. S3I). For instantaneous velocity, in our raw data, the data pointed in Supplementary Fig. S3J were not monotonic, caused by noise. As we know, AP propagation was unidirectional. Therefore, we used least-squares curve fitting with linear constraints to fit the raw data, where C is an identity matrix, x is the unknown monotonic time, d is the raw data (peak arrival time), and the constraint is

$$x_{i+1} - x_i \leq -0.001.$$

$$\min_x \frac{1}{2} \|C \cdot x - d\|^2 \quad s. t. \quad A \cdot x \leq b$$

Generally, in our data, the maximum velocity in the AIS was 300 $\mu\text{m}/\text{ms}$, the minimum distance between two data points was 0.325 μm (the pixel size in the raw imaging data). Thus, the constraint was set to 0.001. In this way, we calculated the monotonic propagation line (Supplementary Fig. S3J). The slope of

the line on each location is the instantaneous velocity. The velocity change per unit distance is the velocity change rate with respect to time.

The spatial and temporal resolutions of the velocity were 0.325 μm (along the propagation direction on the axon) and 0.002 ms, respectively. We defined the propagation velocity as peak propagation velocity. Due to the limitation of the raw data and the data analysis methods, the velocity calculation in the AIS shorter than 20 μm was not precise enough. Therefore, only AISs over 20 μm in length could be quantitatively observed. The data processing code was available on GitHub (<https://github.com/Jessie940611/Action-Potential-Propagation-Velocity-is-Influenced-by-AIS-Plasticity>).

Multi-compartmental modeling

We created a detailed multi-compartment model of a neuron to explore the relationship between AIS plasticity and action potential propagation velocity. The model included simplified morphology, ion channel distributions and densities, channel kinetics, and passive properties. We stimulated the model neuron with a pulse current injected directly into the soma. The simulation was performed by NEURON's (version 7.6.5) Python (version 3.6.6) interface. The integration time steps were fixed at 0.001 ms. The length of the segment was 1 μm . The full model is available on GitHub (<https://github.com/Jessie940611/Action-Potential-Propagation-Velocity-is-Influenced-by-AIS-Plasticity>).

Neuronal morphologies included several simple cylinders to mimic dendrite, soma, hillock, AIS, and axon. Various passive parameter values were explored within physiologically relevant ranges taken from the literature [45, 46]. The specific values of passive parameters were chosen to match the experimentally measured input resistance and membrane time constant in hippocampus neurons. The specific membrane capacitance, specific membrane resistance, intracellular resistivity, and leak current reversal potential were set to 0.5 $\mu\text{F}/\text{cm}^2$, 10000 $\Omega\cdot\text{cm}^2$, 300 $\Omega\cdot\text{cm}$, and -65 mV, respectively. As for the active properties, the gating kinetics of voltage-dependent $\text{Na}_{\text{v}1.2}$, $\text{Na}_{\text{v}1.6}$, and K_{v} channels were Hodgkin-Huxley style [30]. The densities of ion channels were based on previously published values. AIS compartments contained $\text{Na}_{\text{v}1.2}$ and $\text{Na}_{\text{v}1.6}$, and other compartments only contained Na_{v} channels [30, 46, 47]. The parameters are shown in Supplementary Table S2.

Results

Intrinsic excitability increased more sharply with the simulation strength elevation in APP/PS1 mouse hippocampal neuron

As a severe neurodegenerative disorder, AD has destabilized calcium homeostasis and presynaptic/postsynaptic glutamate regulations related to dysfunction of neuronal excitability [48-51]. Axonal pathology in APP/PS1 neurons, accompanied by membrane proteins and ion channel alterations,

could seriously affect intrinsic neuronal excitability [52-55]. In the present study, we found that wild-type neuron and APP/PS1 neurons have normal resting potential (WT: -69.1 ± 0.98 mV, $n = 77$; APP/PS1: -67.1 ± 0.82 mV, $n = 48$, ^{ns}P value = 0.1703) (Fig. 1A). Then, we performed a current injection with small gradual increases (from 5 to 100 pA with a step of 5 pA). The current injection duration and the following rest duration were 500 ms) to investigate the excitability change in different stimulation strengths in wild-type and APP/PS1 neurons. Our results showed that APP/PS1 neurons had significantly higher rheobase under 500 ms depolarizing current injection than wild-type neurons (WT: 50.2 ± 3.7 pA, $n = 52$; APP/PS1: 63.6 ± 4.3 pA, $n = 35$, ^{**}P-value = 0.0057) (Fig. 1B).

APP/PS1 neurons were much more sensitive to the current injection than wild-type neurons and had higher AP frequency when the current injection was strong enough, showing a stimulation-strength-dependent excitability heterogeneity. As shown in Fig. 1C, compared to wild-type neurons (gray), APP/PS1 neurons (green) had lower AP frequency with a lower intensity of current injection (for example, 30 pA) but had higher AP frequency with a higher intensity of current injection (for example, 100 pA). The spiking probability of APP/PS1 neurons obviously increased when the current raised to more than 40 pA and surpassed wild-type neurons when the current was more than 65 pA ($n = 52$) (Fig. 1D). More specifically, two types of neurons' AP frequency showed a similar trend (Fig. 1E). Compared to the wild-type neuron, the AP frequency of APP/PS1 neurons was lower with a milder current injection, but it increased severely when the current injection intensity was over 50 pA. The AP frequency surpassed wild-type neurons when the current injection intensity was over 70 pA (Fig. 1E). As highlighted in Fig. 1F and G, the AP frequency of APP/PS1 neuron was about 60% less than wild-type under 50 pA current injection (WT: 3.49 ± 0.71 Hz, $n = 52$; APP/PS1: 1.32 ± 0.37 Hz, $n = 35$, ^{*}P value = 0.0191) (Fig. 1F), but about 60% more than the wild-type neurons under 100 pA current injection (WT: 6.78 ± 1.03 Hz, $n = 52$; APP/PS1: 10.8 ± 1.31 Hz, $n = 35$; ^{*}P value = 0.0132) (Fig. 1G).

Stimulation-strength-dependent excitability increase not only reflected in the AP frequency but also in the first AP peak latency. It decreased along with the current injection intensity increase, and the gap between the two types of neurons decreased to less than 10 ms when the current injection intensity was over 75 pA (Fig. 1G). The first AP peak latency of APP/PS1 neuron was significantly longer than wild-type neuron when neurons were stimulated by a 50 pA current injection (WT: 149.6 ± 12.4 ms, $n = 28$; APP/PS1: 228.1 ± 28.2 ms, $n = 14$, ^{*}P value = 0.0202) (Fig. 1I), while it was almost equal to wild-type neurons with 100 pA injection (WT: 109.9 ± 10.6 ms, $n = 42$; APP/PS1: 111.3 ± 12.0 ms, $n = 32$, ^{ns}P value = 0.9303) (Fig. 1J). Correspondingly, in APP/PS1 neurons, the time interval between the first and second peak with the increased stepwise current injection also decreased faster than wild-type neurons and was basically the same as wild-type neurons when current injection intensity was over 70 pA (Fig. 1K).

High spatial-temporal voltage imaging was applied to study action potential initiation and propagation in the AIS

To study the AP initiation site and propagation manners in the AIS, we performed voltage imaging in cultured hippocampal neurons from wild-type and APP/PS1 mice. We chose QuasAr2 as the GEVI in this study for its high sensitivity and fast response kinetics [43]. It has been employed to monitor AP initiation in cultured rat hippocampal neurons and investigate neuronal excitability of ALS patient-derived motor neurons [43, 56]. Compared to previous imaging studies of the AIS using dyes [40-42], QuasAr2 offers a superior signal-to-noise ratio (SNR) for its lower background signals and higher sensitivity in responding to AP events and describing the AP waveform details [36, 57].

As showed in Fig. 2A, cultured hippocampal neurons were transfected with QuasAr2-mOrange2 plasmid. They were stimulated by periodic current injections injected into the soma via the whole-cell current clamp. Meanwhile, QuasAr2 fluorescence images of the AIS and adjacent soma, axon, and dendrites were acquired at a 484 Hz camera frame rate. The transfected neurons for voltage imaging from wild-type and APP/PS1 mice showed a significant difference neither in their Full Width at Half Maxima (FWHM) of evoked APs, nor in the amplitude, resting potential, or threshold potential (Supplementary Fig. S1). After the voltage imaging, we used the standard immunofluorescence (IF) technique to visualize the recorded neurons and their AIS. The neurons were filled with biocytin (0.5% w/v) as a tracer, and the AIS-localized AnkG or NF186 indicated their AISs. (Fig. 2A and B; Supplementary Fig. S2).

We generated the spike-triggered average movies from the voltage imaging results corresponding to the current injection-induced AP trains (Fig. 2C). The optical signals of APs in the spike-triggered averaged movies had much higher SNR, and a few AP propagations could be directly observed from the movie (Fig. 2D). In our experiment results, the current injection (10 ms - 150 pA stimulation, frequency = 6.25 Hz, and total AP number = 125) generated AP trains and corresponding fluorescence of QuasAr2 changed in the soma, AIS, and axon (outlined in blue, orange and yellow, respectively) (Fig. 2D). The fluorescence intensity robustly reported AP spikes at the AIS and neighboring regions, with an SNR ranging between 11 and 36 in the outlined AIS region (Fig. 2D, center column, mean \pm standard deviation: 17.2 ± 4.3). We generated the spike-triggered average spike movie to boost the SNR of the AP signal in the AIS to 111 (Fig. 2D, right column, the AIS trace). We further adapted an upsampling algorithm [42, 43] to analyze the AP timing with sub-millisecond-level temporal resolution and pixel-level spatial resolution (Fig. 2E and Supplementary Fig. S3, see METHODS). After this processing, we identified the AP initiation site and the velocity of bidirectional AP propagation in the AIS and adjacent soma, axon, and dendrites (Fig. 2F).

Voltage imaging reveals AP propagation velocity at the AIS

In our study, *AIS length* was defined as the distance between the *proximal end* and *distal end* of the AIS, and *AIS location* was defined as the distance from cell soma to the AIS proximal end [58]. Since its initiation, AP propagates bi-directionally, with *forward-propagating action potentials (fpAPs)* traveling along the axon and *back-propagating action potentials (bpAPs)* towards the soma and the dendrites (Fig. 3A). The previously described voltage imaging technique and data processing algorithm (Fig. 2E and f and Supplementary Fig. S3) generated a pixel-by-pixel AP firing timing heatmap (Fig. 3B). We extracted

the mean AP propagation velocities on several compartments with high temporal-spatial resolution from our raw data (Fig. 3C). We measured AP velocities in the AIS and compared these values pairwise. We found that the velocity of fpAP in the AIS was (1.87 ± 0.39 times) faster than in the axon ($119.5 \pm 18.7 \mu\text{m/ms}$ and $73.45 \pm 7.76 \mu\text{m/ms}$, respectively, *P-value = 0.0214) (Fig. 3D). We also found that the velocity of fpAPs were generally faster (1.51 ± 0.18 times) than the corresponding bpAPs ($112.6 \pm 14.2 \mu\text{m/ms}$ and $84.99 \pm 7.59 \mu\text{m/ms}$, respectively, ^{ns}P value = 0.0547) (Fig. 3E). Taken together, our voltage imaging method enabled us to distinguish AP propagation velocities from different subcellular regions.

It is well established that the AIS is a highly structured region and is attached by many ion channels, playing a crucial role in the AP initiation and propagation. This high spatial and temporal resolution technique allowed us to observe the changes in AP velocity during the propagation. As shown in Fig. 3F, the raw peak arrival times (gray circles) were not monotonic because of the data noise. Thus, we used the least-squares curve fitting with linear constraints to fit the raw data. Lines in Fig. 3F indicated the monotonic data; the slopes of lines on each location were the instantaneous velocities (Fig. 3G). The velocity sign represented the propagation direction; negative and positive velocities were bpAP and fpAP velocities, respectively. The velocity change per unit time was the acceleration (Fig. 3H). The sign of acceleration represented if the velocity becomes slower or faster. For bpAP, the maximum acceleration (the blue triangle) was where bpAP speeded up most, while the minimum acceleration (the blue inverted triangle) was where bpAP slowed down most. For fpAP, the maximum acceleration (the brown triangle) was where fpAP speeded up most, while the minimum acceleration (the brown inverted triangle) was where fpAP slowed down most. Here we defined SDMP as the point where AP slowed down most and SUMP as the point where AP speeded up most.

The calculation details of the acceleration are mentioned in the METHODS section. We calculated SDMP and SUMP on all neurons. In the control group, the relative distance from SDMP and SUMP of bpAP to the AIS proximal end (SDMP/SUMP - AIS proximal end) was $3.8 \pm 0.6 \mu\text{m}$ ($n = 64$) and $4.3 \pm 0.6 \mu\text{m}$ ($n = 64$), the location distribution was present in the histogram (Fig. 3I and J). The relative distance from SDMP and SUMP of fpAP to the AIS distal end (SDMP/SUMP - AIS distal end) was $-1.3 \pm 0.7 \mu\text{m}$ ($n = 64$) and $-1.8 \pm 0.6 \mu\text{m}$ ($n = 64$); histogram shows the location distribution (Fig. 3K and L). These results indicated that the AP velocity had a sudden change near the proximal and distal end of AIS. It suggests a specific morphological structure in the AIS, not only the selective transportation of the molecules at the terminal of the AIS, but the structure affects the AP propagation properties.

AP was initiated more distal to the soma in APP/PS1 neurons

Previously we showed that APP/PS1 mouse model had axon abnormalities with shortened AIS mediated by AnkG down-regulation [9]. We identified the AIS with AnkG as a marker (Fig. 4A). We set the highest fluorescence value of AnkG along the axon as the maximum (100%) fluorescence intensity and the lowest fluorescence value of AnkG as the minimum (0%) fluorescence intensity. We defined the region with more

than 10% of the maximum fluorescence intensity as the AIS proximal and distal end [58]. Compared to wild-type neurons, the AIS of APP/PS1 hippocampal neurons had similar location (WT: $5.904 \pm 0.77 \mu\text{m}$; APP/PS1: $5.383 \pm 1.05 \mu\text{m}$, ^{ns}P-value = 0.6857) (Fig. 4B), but had significantly shorter length (WT: $38.49 \pm 1.86 \mu\text{m}$; APP/PS1: $24.07 \pm 1.07 \mu\text{m}$, ^{***}P-value < 0.001) (Fig. 4C).

To obtain the detailed AP initiation and propagation information, we extracted the AP propagation process from raw data and defined the location with the earliest action potential peak time as the AP initiation site (red dot in Fig. 3C). We first normalized each AIS length from *proximal end* (0%) to *distal end* (100%) and calculated the relative AP initiation site. We found that in wild-type neurons, the highest probability of AP initiation site was at 50%-70% of total AIS length, which was coincided not only with the spatial distribution of voltage-gated sodium channel $\text{Na}_{v1.6}$ in the AIS, but also with the findings of the previous study that AP is initiated in the slightly distal end of the AIS [30, 59]. However, in APP/PS1 neurons, APs were initiated more distally (70%-90% of total AIS length), even one-third of neurons-initiated AP in the axon area distal to the AIS (Fig. 4D). Nevertheless, APs were nearly initiated at the same absolute distance to the soma in wild-type and APP/PS1 neurons (Fig. 4E and F). In addition, the correlation analysis showed that in wild-type neurons, when the AIS was located distal to the soma, AP further tended to the soma ($n = 17$) (Fig. 4G). This positive correlation was more apparent between the AP absolute initiation site and AIS length ($n = 17$) (Fig. 4H). However, in APP/PS1 neurons, although the absolute AP initiation site was similar to wild-type neurons, the correlations between absolute AP initiation site and AIS location or length were both disturbed ($n = 11$) (Fig. 4I and J).

The alteration of AIS length and sodium channel decreased AP velocities in APP/PS1 neuron

The velocity of AP propagation significantly affects the approach timing of the electrical signals, which is the key to trigger neurotransmitter release at the axon terminals and integrate the information at the soma [23-28]. Since APP/PS1 neurons showed apparent AP initiation alteration, the AP propagation patterns in APP/PS1 neurons might be different from those in wild-type neurons. To study whether AIS structural alteration in APP/PS1 neurons also affected AP propagation, we directly recorded AP propagation velocity in the AIS via the high spatial-temporal voltage imaging. We measured AP velocities in the AIS and found that both bpAP (WT: $132.5 \pm 10.33 \mu\text{m}/\text{ms}$; APP/PS1: $77.49 \pm 11.55 \mu\text{m}/\text{ms}$, ^{**}P-value = 0.0016) and fpAP (WT: $90.42 \pm 8.45 \mu\text{m}/\text{ms}$; APP/PS1: $66.42 \pm 6.51 \mu\text{m}/\text{ms}$, ^{*}P-value = 0.0254) velocities in APP/PS1 neurons were lower than the wild-type neurons (Fig. 5A and B). The correlation analysis of the AP initiation site and AP velocities showed that in wild-type neurons, neither bpAP ($n = 18$) nor fpAP velocity ($n = 13$) were correlated with its initiation site, so did APP/PS1 neurons ($n = 11$ and $n = 9$, respectively) (Fig. 5C and D), suggesting the AP initiation site fluctuation did not affect its propagation velocities.

To study whether the shorter AIS in APP/PS1 neurons reduced the AP propagation velocities in the AIS, we analyzed the correlation between the AIS location/length and bpAP/ fpAP velocities. In wild-type

neurons, the bpAP velocity ($n = 18$) was not affected by the AIS location (Fig. 5E), but was slightly reduced in the longer AIS (Fig. 5F). In contrast, the velocity of fpAP ($n = 12$) significantly decreased in the AIS located far from the soma or in the shorter AIS (Fig. 5G and H). According to these observations, the APP/PS1 neuron has a shorter AIS with a similar location than the wild-type neuron. The lower fpAP velocity was consistent with the correlation between fpAP velocity and AIS length, not the bpAP. These results suggest that in APP/PS1 neurons, the decreased AP velocities in the AIS and neighbor compartments were not uniquely related to the AIS length but might also be contributed to other parameters. We also analyzed the correlation in APP/PS1 neurons, but those correlations were not appeared in APP/PS1 neurons (bpAP: $n = 12$ and fpAP: $n = 9$, respectively) (Fig. 5I-L).

The AIS was shorter in APP/PS1 neurons, and $\text{Na}_{v1.6}$ was distributed along the entire axon and showed a lower proportion in the AIS region. We constructed two multi-compartment models to verify whether these changes lead to the bpAP and fpAP velocities decrease in APP/PS1 neurons, one simulated wild-type neuron (Fig. 5M), and the other simulated APP/PS1 neuron (Fig. 5N). Both models were composed of several sections: dendrite, soma, hillock, AIS, and axon. We adjusted the model's morphological and physical parameters according to the published studies [9, 45-47, 60]. Compared with the wild-type neuron model, the length of the AIS segment in the APP/PS1 neuron model was set shorter, the sodium channel density in the AIS segment was set lower, and the sodium channel density in the axon segment was set higher than wild-type neuron model. The specific parameters are listed in Supplementary Table S2. We injected the same current (1 nA, 1 ms) into the soma section. Each section contained some compartments, and the length of each compartment was 1 μm . Fig. 5M and N showed the AP peak arrival time of each compartment. The slopes of the dotted arrows showed the mean velocity of bpAP and fpAP in the AIS. In the simulation, the bpAP and fpAP velocities in APP/PS1 neuron model (bpAP: 125.0 $\mu\text{m}/\text{ms}$; fpAP: 166.7 $\mu\text{m}/\text{ms}$) were both lower than wild-type neuron model (bpAP: 144.7 $\mu\text{m}/\text{ms}$; fpAP: 185.2 $\mu\text{m}/\text{ms}$). These simulation results reproduced the experiment conclusions, indicating that the shorter AIS and the abnormal location of sodium channels together decreased AP velocities in the APP/PS1 neuron.

fpAP propagation velocity was influenced by the AIS length and location

Our study uncovered that fpAP velocity significantly correlated with AIS location and length (Fig. 5G and H). To further investigate the relationship between fpAP velocity and AIS location, we pharmacologically perturbed the AIS location in wild-type neurons. A previous study showed that treating mature AIS (after DIV7) with 15 mM KCl for 48 hours significantly shifted the AIS distally without affecting the AIS length [58]. Therefore, we employed this method to induce an AIS location shift.

In the untreated neuron, the velocity of bpAP ($n = 30$) slightly decreased in AIS either was located far from the soma or longer. However, neither of them showed statistical significance (Fig. 6A and B). In contrast, the velocity of fpAP ($n = 19$) was negatively correlated to the AIS location and positively correlated to the

AIS length (Fig. 6C and D). After 15 mM KCl treatment from DIV10 to DIV12, the resting potential of these neurons did not change (Fig. 6E), while the rheobase current significantly increased when the neurons were moved back to the 2.5 mM K⁺ extracellular medium (Fig. 6F).

As envisioned, the AIS location was considerably moved away from the soma (Fig. 6G and H), while the AIS length did not change (Fig. 6G, I). Consistent with the above observations (Fig. 6A-D), bpAP velocity barely changed ($101.3 \pm 8.87 \mu\text{m}/\text{ms}$ and $83.74 \pm 13.89 \mu\text{m}/\text{ms}$, respectively, ^{ns}P value = 0.2676) (Fig. 6J), and fpAP velocity was much lower ($138.8 \pm 20.1 \mu\text{m}/\text{ms}$ and $65.33 \pm 9.30 \mu\text{m}/\text{ms}$, respectively, ^{**}P-value = 0.0028) (Fig. 6K), when compared to the untreated neurons. Moreover, in the KCl-treatment group, the velocity of bpAP (n = 15) was not significantly influenced by AIS location and length (Fig. 6L and M). In contrast, the velocity of fpAP (n = 10) was negatively correlated with AIS location and positively correlated to AIS length (Fig. 6N and O), consistent with the correlations in the untreated neurons (Fig. 6A-D). Taken together, the AIS distally shifting did not significantly influence the bpAP velocity in the AIS, but significantly affected the fpAP velocity in the AIS. These results demonstrated that the AIS location and length influenced the fpAP velocity.

Sodium channel distribution determined the correlation between AIS location/length and AP propagation velocities

To quantitatively study neuronal propagation velocity, we constructed a multi-compartment model. Our model consisted of several sections: dendrite, soma, hillock, AIS, and axon. For simplicity, we modeled each section as a cylinder (Fig. 7A). The model included four types of ionic currents: I_{Nav} , $I_{\text{Nav}1.2}$, $I_{\text{Nav}1.6}$, and I_{Kv} . The AIS contained $I_{\text{Nav}1.2}$, $I_{\text{Nav}1.6}$, and I_{Kv} , but not I_{Nav} ; all other sections contained I_{Nav} and I_{Kv} . Furthermore, the AIS had higher current densities than the other sections, consistent with previous observations. The stimuli injected in the middle of the soma was a pulse current (1 ms, 1 nA).

To examine the mechanisms underlying the correlation between AIS location/length and AP propagation velocities in our experiments (Fig. 6A-D), we explored many parameters in our model. We found parameter regimes where the model qualitatively reproduced experimentally observed trends. Among all the parameters, we found that the spatial distribution of sodium channels most robustly affected the trends. Here we demonstrated the effect by comparing two specific types of sodium channel distribution in the AIS. The default, Type 1 (left panel in Fig. 7B), was a uniform distribution. However, as described in previous studies, the densities of $\text{Na}_{\text{v}1.2}$ and $\text{Na}_{\text{v}1.6}$ were not uniform. Therefore, in Type 2 (right panel in Fig. 7B), we modeled $\text{Na}_{\text{v}1.2}$ to have a higher density in the proximal AIS and $\text{Na}_{\text{v}1.6}$ to higher density in the distal AIS. As shown in Fig. 7C, when the distribution of sodium channels was set to be uniform (Type 1), bpAP propagated slightly lower in the AIS located distally, consistent with our experimental results. However, bpAP propagated faster in longer AIS, which contrasts with the experimental results. Moreover, the dependencies of fpAP velocities in the AIS location and length were all inconsistent with our experimental observations.

However, if sodium channels were distributed as Type 2, we could reproduce many experimental trends. For example, in Type 2 sodium channel distributions simulations, bpAP propagated slightly lower in the AIS located distally. Furthermore, modeling results demonstrated that the longer the AIS was, the faster the fpAP propagated. These conclusions were consistent with the experimental results. Compared to Type 1, in Type 2 AISs, the fpAP velocity was not higher in the AIS located distally, and the bpAP velocity had no uniform correlation with AIS length. These conclusions are similar to the experimental trends in Type 2 than in Type 1. In addition to these two types of sodium channel distributions, we tried other types of sodium channel distributions, as shown in Supplementary Fig. S4A-D. Their corresponding simulation results were similar to Type 2 (Supplementary Fig. S5).

Type 2 simulation results could not completely reproduce the experimental trends due to the complexity of soma-to-dendritic morphology in neurons. Soma-to-dendritic morphology influences neuronal physiology, weakening the correlation between AIS plasticity and AP velocities. Furthermore, in our models, as long as the proximal AIS had higher $\text{Na}_{v1.2}$ densities than the distal AIS and distal AIS had higher $\text{Na}_{v1.6}$ densities than the proximal AIS, simulation results can reproduce many experimental results. Therefore, we concluded that sodium channel distribution significantly influenced the interaction between AIS length/location and AP propagation velocities. These simulations suggested that the change in the correlation between AIS location/length and AP propagation velocities in APP/PS1 neurons to wild-type neurons might due to the sodium channel disorganization attributed to axon pathology.

Finally, to study the effect of ion channel densities on AP propagation velocities, we adjusted $g_{\text{Nav}1.2}$, $g_{\text{Nav}1.6}$, and g_{K} , respectively, keeping to a Type 2 sodium distribution (Supplementary Fig. S6). We found that densities of $\text{Na}_{v1.2}$ and $\text{Na}_{v1.6}$ hardly affected neither the AP velocities nor the trends of how bpAP and fpAP velocities varied with AIS location and length. However, the density of K_v affects the AP velocities the most (generally, a higher K_v density led to lower bpAPs and faster fpAPs) but hardly affected how bpAP and fpAP velocities varied with AIS location and length. These results suggested that the ion channels' spatial distribution, but not its densities on specific sites, more strongly influenced the interaction between AIS length/location and AP propagation velocities.

Discussion

As an important axonal region, the AIS regulates neuronal excitability and is the initiation site of APs. Our data suggested that compared to wild-type hippocampal mouse neurons, the neurons from APP/PS1 mice were with a significantly higher rheobase during a 500 ms depolarizing stepwise current injection and were with a significant lower AP frequency and a longer AP latency when facing a moderate injection intensity around the rheobase (Fig. 1B, E, and H). However, when the current injection intensity increased, APP/PS1 neurons reflected a sharper excitability elevation in the higher AP frequency and the lower first AP peak latency (Fig. 1D-J). Under the 100 pA current injection intensity, the APP/PS1 neuron represented much higher excitability, especially in a higher AP firing frequency (60% more than the wild-type neurons) (Fig. 1D, E, and G). The elevation in the expression of voltage-gated sodium channels, especially the

lower-threshold $\text{Na}_{v1.6}$ channel, was reported in the APP/PS1 mouse neurons [61]. Even the treatment of exogenous soluble $\text{A}\beta_{1-42}$, which is the main secreted marker in the brain of AD patients, could also increase the $\text{Na}_{v1.6}$ channel expression level. Previous studies showed increased excitability in mature cultured APP/PS1 neurons with the increased expression levels of sodium channels, especially the AIS-localized $\text{Na}_{v1.6}$ channel [52, 54, 62, 63]. These neurons were reported with a higher AP firing frequency and a lower threshold upon injecting a strong depolarizing current (i.e., 200 pA, 500 ms). Incubation of soluble $\text{A}\beta_{1-42}$ could also alter neuronal excitability in cultured mouse cortical neurons or hippocampal pyramidal neurons via elevating the expression of $\text{Na}_{v1.6}$ or persistent sodium currents, respectively [52, 64]. Therefore, we suspected that in APP/PS1 mice neurons, the heterogeneous expression level and distribution of $\text{Na}_{v1.6}$ channel and other molecular and structural changes in the AIS could also lead to the diversity in the initiation site propagation style of action potentials.

On the other hand, rodents and human $\text{A}\beta$ modulate the current densities of various voltage-gated potassium channels, which may synergistically influence the AP frequency and latency of APP/PS1 neurons with different current injection intensities [65-67]. However, these results cannot directly elucidate the lower excitability of APP/PS1 neurons with milder current injection. Considering the immense structural and molecular changes in the AIS of APP/PS1 mice, we suggested that other factors in the AIS may induce the stimulation-strength-dependent intrinsic excitability difference in APP/PS1 neurons. Besides intrinsic neuronal excitability, we found that the low-threshold $\text{Nav}1.6$ channel was vital in determining the action potential initiation site in the AIS [30, 68-70]. Previous studies have reported that in the APP/PS1 neurons, the $\text{Na}_{v1.6}$ channel is in overexpression and dislocation along the entire axon, but not the distal AIS in the wild-type neurons [9]. In addition, abnormal Na^+ channel distribution is a critical factor of seizure, a common symptom observed in AD patients as a comorbidity widely reported [71-74]. The early-onset familial AD is linked to an 87-fold rise in seizure incidence compared with the general population [75]. A recent study suggested epileptiform activity accelerates AD onset, and the evidence from a sporadic AD patients study showed a relationship of electroencephalography (EEG) abnormalities with an earlier onset of AD and faster progression of clinical impairment [76]. Therefore, this evidence suggests that a therapeutic strategy targeting the Na^+ channel in the early stage AD patients may postpone AD complications such as seizures.

We screened the AP initiation site and AP velocities during the bidirectional propagation in the AIS and adjacent regions using the high spatial-temporal voltage imaging technique. Compared to other techniques recently used in studying AP propagation in the AIS like high-density microelectrode array (HD-MEA) [77, 78] or intracellular or extracellular recording technique [34, 79], the optical method (voltage imaging) is believed to have a better spatial resolution, higher sampling density (more individual acquisition points in the AIS). It has already been used to evaluate “sub-frame level” action potential details [43, 80-82]. As mentioned earlier, *in situ* interrogation of AP propagation in the AIS via multi-electrode intracellular patch-clamp recording has remained a technical challenge, so we cannot directly validate our method via electrodes-based “gold-standard techniques” in the AIS and neighbor compartments [29, 83]. Our results might differ from recently reported data via other techniques. A

previous extracellular-recording study at 37°C showed that the average bpAP velocity in the AIS was $1100 \pm 1500 \mu\text{m/ms}$ (mean \pm s.d.), with a median velocity of $600 \mu\text{m/ms}$ [79]. Our data, which were acquired at room temperature (22°C), showed the bpAP velocity was $88.02 \pm 7.02 \mu\text{m/ms}$ (mean \pm s.e.m.), and the fpAP velocity was $120.7 \pm 13.8 \mu\text{m/ms}$ (mean \pm s.e.m.), lower than the previous data. The difference in velocity may be due to the temperature difference. Another study based on HD-MEA recording showed that AP propagation velocity in the proximal axon of cultured neurons would decrease at least 60% when the temperature was down to 22°C from 37°C. The other possible reason is the difference in the spatial resolution of the various techniques used in the studies mentioned earlier. According to Bakkum *et al.* [32, 79], the costumed HD-MEA they used is composed of electrodes with $17.8 \mu\text{m}$ pitch and $8.2 \times 5.8 \mu\text{m}^2$ area (3150 individual acquisition points per mm^2), which might be not able to capture the electrical activity details in the entire AIS because of the too large electrode size and pitch (few electrodes could record the signal belonging to the AIS). In our voltage imaging setup, the area of individual acquisition units (pixels) is about $0.325 \times 0.325 \mu\text{m}^2$ (9.5 million acquisition points per mm^2). Thus, we could get about 100 unique data points to measure the action potential and calculate the propagation, so the improved data sampling density may also distinguish between the velocity results in the AIS.

As a severe neurodegenerative disorder, AD is associated with neuronal cytoskeletal alterations and axon pathology, which is highly related to the loss of dendritic spines and synapses and neuronal degeneration [3-7]. Our previous study showed an AIS structure transformation in the APP/PS1 mouse neurons, but how the AIS structure alteration causes neuronal function defects in the AD model remains unknown [9]. Taking advantage of the recent development of sensitive fluorescent voltage indicators and advanced data processing methods, we now observe the point of AP initiation within the AIS region and comprehensively describe how the AP propagates towards the cell body and the axonal terminal. We found that the highest AP initiation occurrence in wild-type neurons was at 50%-70% of the AIS length (Fig. 4D), consistent with the previous study [30]. However, in the APP/PS1 neurons, the AP initiation site was a significantly distal shift, and even 30% of APs initiated in the axon (Fig. 4D). The shift may be attributed to the distribution change of the low threshold voltage-gated sodium channel $\text{Na}_{\text{v}1.6}$, which is down-regulated in the AIS and distributed along the entire axon. The pathological distribution of $\text{Na}_{\text{v}1.6}$ may be the most critical factor of epilepsy, which was common comorbidity widely reported recently [71-74]. The early-onset familial AD is linked to an astonishing 87-fold rise in seizure incidence compared with the general population [75].

The structural changes of cytoskeleton proteins and adaptor proteins will alter the density, location, and interaction of these ion channels, leading to changes in neuronal excitability. In our study, although the AIS length was much shorter in APP/PS1 neurons than that in wild-type neurons, the AP's initiation site shared a similar distance from the soma with wild-type neurons. Meanwhile, compared to the wild-type neuron, APP/PS1 neurons showed a low AP spiking frequency under lower current injection but a much higher AP spiking frequency when the injection intensity increased. This may be attributed to the disturbance of ion channel homeostasis in their expression and distribution, resulting in a lower AP propagation velocity in the AIS and abnormal neuronal function. It is noteworthy that these results were

derived from postnatal day 0 mice neurons, suggesting that for familial AD, there were significant changes in neuronal excitability and AP conduction velocity long in the neurons before the onset of AD symptoms. This pathological process is a long way away from sporadic AD, through AIS pathology to white matter lesions. Meanwhile, we also have reasons to believe that changes in neuronal excitability and AP dynamics can be observed long before the symptoms appeared, suggesting that using electroencephalography (EEG) to assist diagnosis in suspected AD patients may help to diagnose AD relative patients in an early stage. Therefore, this evidence suggests that a therapeutic strategy targeting the sodium channels in the early-stage AD patients may postpone AD complications, such as seizures.

Declarations

Funding:

This work was supported by the National Science Foundation of China (NSFC) major research grant (31630028, 91632305, and 91753131), NSFC general research grant (81971679, 21673009, 21727806, and 31771147), and the Natural Science Foundation of Beijing Municipality (5182011). P.Z. is supported by the National Thousand Young Talents Award and Li Ge-Zhao Ning Life Science Junior Research Fellowship.

Competing interests:

All authors declare no actual or potential conflicts of interest, including any financial, personal or other relationships, with other people or organizations within three years of beginning the work submitted that could inappropriately influence (bias) their work

Availability of supporting data and materials:

The original data and materials are available upon request.

Code availability:

The custom code is available upon request.

Authors' contributions:

Z.C., L.P., and M.Z. performed all experiments and analyzed the data. Y.Z., P.Z., and L.T. conceptualized the study, performed analyses, and drafted the manuscript with inputs from all authors. All authors read and approved the final manuscript.

Ethical Approval and Consent to participate:

Animal materials were from Beijing Vital River Laboratory Animal Technology Co., Ltd., and experimental procedures were following the rules and regulations of Peking University Animal Care and Use Committee.

Consent for publication:

All involved parties consented to publication of this manuscript

Acknowledgements

We thank the assistance of the National Center for Protein Sciences at Peking University in Beijing, China, and the State Key Laboratory of Membrane Biology at Peking University in Beijing, China. In addition, we thank Dr. Yulong Li and Donggen Luo for their valuable feedback on the manuscript.

References

1. Kukull WA, Bowen JD (2002) Dementia epidemiology. *Medical Clinics* 86(3):573–590
2. Price DL, Sisodia SS, Gandy SE (1995) Amyloid beta amyloidosis in Alzheimer's disease. *Curr Opin Neurol* 8(4):268–274
3. Braak H, Braak E (1995) Staging of alzheimer's disease-related neurofibrillary changes. *Neurobiol Aging* 16(3):271–278
4. Adalbert R, Nogradi A, Babetto E, Janeckova L, Walker SA, Kerschensteiner M, Misgeld T, Coleman MP (2008) Severely dystrophic axons at amyloid plaques remain continuous and connected to viable cell bodies. *Brain* 132(2):402–416
5. Merino-Serrais P, Benavides-Piccione R, Blazquez-Llorca L, Kastanauskaite A, Rábano A, Avila J, DeFelipe J (2013) The influence of phospho-tau on dendritic spines of cortical pyramidal neurons in patients with Alzheimer's disease. *Brain* 136(6):1913–1928
6. Spires TL, Meyer-Luehmann M, Stern EA, McLean PJ, Skoch J, Nguyen PT, Bacskai BJ, Hyman BT (2005) Dendritic Spine Abnormalities in Amyloid Precursor Protein Transgenic Mice Demonstrated by Gene Transfer and Intravital Multiphoton Microscopy. *The Journal of Neuroscience* 25(31):7278–7287
7. Vickers JC, King AE, Woodhouse A, Kirkcaldie MT, Staal JA, McCormack GH, Blizzard CA, Musgrove REJ, Mitew S, Liu Y et al (2009) Axonopathy and cytoskeletal disruption in degenerative diseases of the central nervous system. *Brain Res Bull* 80(4):217–223
8. Blazquez-Llorca L, Valero-Freitag S, Rodrigues EF, Merchán-Pérez Á, Rodríguez JR, Dorostkar MM, DeFelipe J, Herms J (2017) High plasticity of axonal pathology in Alzheimer's disease mouse

- models. *Acta Neuropathologica Communications* 5(1):14
9. Sun X, Wu Y, Gu M, Liu Z, Ma Y, Li J, Zhang Y: **Selective filtering defect at the axon initial segment in Alzheimer's disease mouse models.** *Proceedings of the National Academy of Sciences* 2014:201411837
 10. Grubb MS, Burrone J (2010) Building and maintaining the axon initial segment. *Curr Opin Neurobiol* 20(4):481–488
 11. Rasband MN (2010) The axon initial segment and the maintenance of neuronal polarity. *Nat Rev Neurosci* 11(8):552–562
 12. Huang CY-M, Rasband MN (2018) Axon initial segments: structure, function, and disease. *Ann N Y Acad Sci* 1420(1):46–61
 13. Buffington SA, Rasband MN (2011) The axon initial segment in nervous system disease and injury. *Eur J Neurosci* 34(10):1609–1619
 14. Clark BD, Goldberg EM, Rudy B (2009) Electrogenic tuning of the axon initial segment. *The Neuroscientist* 15(6):651–668
 15. Bender KJ, Trussell LO (2012) The physiology of the axon initial segment. *Annu Rev Neurosci* 35:249–265
 16. Kole MH, Stuart GJ (2012) Signal processing in the axon initial segment. *Neuron* 73(2):235–247
 17. Waters J, Schaefer A, Sakmann B (2005) Backpropagating action potentials in neurones: measurement, mechanisms and potential functions. *Prog Biophys Mol Biol* 87(1):145–170
 18. Häusser M, Spruston N, Stuart GJ (2000) Diversity and Dynamics of Dendritic Signaling. *Science* 290(5492):739–744
 19. Bashir ZI, Collingridge GL (1992) Synaptic plasticity: long-term potentiation in the hippocampus. *Curr Opin Neurobiol* 2(3):328–335
 20. Morris R (1989) Synaptic plasticity and learning: selective impairment of learning rats and blockade of long-term potentiation in vivo by the N-methyl-D-aspartate receptor antagonist AP5. *J Neurosci* 9(9):3040–3057
 21. Kamal A, Biessels G-J, Urban I, Gispen W (1999) Hippocampal synaptic plasticity in streptozotocin-diabetic rats: impairment of long-term potentiation and facilitation of long-term depression. *Neuroscience* 90(3):737–745
 22. Voronin L (1993) On the quantal analysis of hippocampal long-term potentiation and related phenomena of synaptic plasticity. *Neuroscience* 56(2):275–304
 23. Rama S, Zbili M, Debanne D (2018) Signal propagation along the axon. *Curr Opin Neurobiol* 51:37–44
 24. Alle H, Geiger JRP (2006) Combined Analog and Action Potential Coding in Hippocampal Mossy Fibers. *Science* 311(5765):1290–1293
 25. Kole MHP, Letzkus JJ, Stuart GJ (2007) Axon Initial Segment Kv1 Channels Control Axonal Action Potential Waveform and Synaptic Efficacy. *Neuron* 55(4):633–647

26. Shu Y, Hasenstaub A, Duque A, Yu Y, McCormick DA (2006) Modulation of intracortical synaptic potentials by presynaptic somatic membrane potential. *Nature* 441(7094):761–765
27. Debanne D (2004) Information processing in the axon. *Nat Rev Neurosci* 5(4):304–316
28. Schmidt-Hieber C, Jonas P, Bischofberger J (2008) Action potential initiation and propagation in hippocampal mossy fibre axons. *The Journal of Physiology* 586(7):1849–1857
29. Hu W, Shu Y (2012) Axonal bleb recording. *Neuroscience Bulletin* 28(4):342–350
30. Hu W, Tian C, Li T, Yang M, Hou H, Shu Y (2009) Distinct contributions of Na(v)1.6 and Na(v)1.2 in action potential initiation and backpropagation. *Nat Neurosci* 12(8):996–1002
31. Li J, Deng S, He Q, Ke W, Shu Y (2021) Asynchronous Glutamate Release at Autapses Regulates Spike Reliability and Precision in Mouse Neocortical Pyramidal Cells. *Cereb Cortex* 31(4):2278–2290
32. Bakkum DJ, Frey U, Radivojevic M, Russell TL, Müller J, Fiscella M, Takahashi H, Hierlemann A (2013) Tracking axonal action potential propagation on a high-density microelectrode array across hundreds of sites. *Nat Commun* 4(1):2181
33. Emmenegger V, Obien MEJ, Franke F, Hierlemann A: **Technologies to Study Action Potential Propagation With a Focus on HD-MEAs**. *Frontiers in Cellular Neuroscience* 2019, 13(159)
34. Abbott J, Ye T, Krenek K, Gertner RS, Ban S, Kim Y, Qin L, Wu W, Park H, Ham D (2020) A nanoelectrode array for obtaining intracellular recordings from thousands of connected neurons. *Nature Biomedical Engineering* 4(2):232–241
35. Ronchi S, Fiscella M, Marchetti C, Viswam V, Müller J, Frey U, Hierlemann A: **Single-Cell Electrical Stimulation Using CMOS-Based High-Density Microelectrode Arrays**. *Frontiers in Neuroscience* 2019, 13(208)
36. Xu Y, Zou P, Cohen AE (2017) Voltage imaging with genetically encoded indicators. *Curr Opin Chem Biol* 39:1–10
37. Peng L, Xu Y, Zou P (2017) Genetically-encoded voltage indicators. *Chin Chem Lett* 28(10):1925–1928
38. Knöpfel T, Song C (2019) Optical voltage imaging in neurons: moving from technology development to practical tool. *Nat Rev Neurosci* 20(12):719–727
39. Liu P, Miller EW (2020) Electrophysiology, Unplugged: Imaging Membrane Potential with Fluorescent Indicators. *Acc Chem Res* 53(1):11–19
40. Antic SD (2003) Action Potentials in Basal and Oblique Dendrites of Rat Neocortical Pyramidal Neurons. *The Journal of Physiology* 550(1):35–50
41. Foust A, Popovic M, Zecevic D, McCormick DA (2010) Action Potentials Initiate in the Axon Initial Segment and Propagate through Axon Collaterals Reliably in Cerebellar Purkinje Neurons. *The Journal of Neuroscience* 30(20):6891–6902
42. Popovic MA, Foust AJ, McCormick DA, Zecevic D (2011) The spatio-temporal characteristics of action potential initiation in layer 5 pyramidal neurons: a voltage imaging study. *The Journal of Physiology* 589(17):4167–4187

43. Hochbaum DR, Zhao Y, Farhi SL, Klapoetke N, Werley CA, Kapoor V, Peng Z, Kralj JM, Maclaurin D, Smedemarkmargulies N (2014) All-optical electrophysiology in mammalian neurons using engineered microbial rhodopsins. *Nat Methods* 11(8):825–833
44. Cui J, Wang Y, Dong Q, Wu S, Xiao X, Hu J, Chai Z, Zhang Y (2011) **Morphine protects against intracellular amyloid toxicity by inducing estradiol release and upregulation of Hsp70.** *J Neurosci* 31(45):16227–16240
45. Mainen ZF, Sejnowski TJ: **Modeling active dendritic processes in pyramidal neurons.** *Methods in neuronal modeling* 1998:171–210
46. Saraga F, Wu C, Zhang L, Skinner F (2003) Active dendrites and spike propagation in multicompartiment models of oriens-lacunosum/moleculare hippocampal interneurons. *J Physiol* 552(3):673–689
47. Kim S, Guzman SJ, Hu H, Jonas P (2012) Active dendrites support efficient initiation of dendritic spikes in hippocampal CA3 pyramidal neurons. *Nature neuroscience* 15(4):600–606
48. Wang R, Reddy PH (2017) Role of Glutamate and NMDA Receptors in Alzheimer's Disease. *J Alzheimers Dis* 57:1041–1048
49. Sushma MAC (2019) Role of GPCR signaling and calcium dysregulation in Alzheimer's disease. *Mol Cell Neurosci* 101:103414
50. Hynd MR, Scott HL, Dodd PR (2004) Glutamate-mediated excitotoxicity and neurodegeneration in Alzheimer's disease. *Neurochem Int* 45(5):583–595
51. Popugaeva E, Pchitskaya E, Bezprozvanny I (2017) Dysregulation of neuronal calcium homeostasis in Alzheimer's disease – A therapeutic opportunity? *Biochem Biophys Res Commun* 483(4):998–1004
52. Wang X, Zhang X-G, Zhou T-T, Li N, Jang C-Y, Xiao Z-C, Ma Q-H, Li S: **Elevated Neuronal Excitability Due to Modulation of the Voltage-Gated Sodium Channel Nav1.6 by A β 1 – 42.** *Frontiers in Neuroscience* 2016, **10**(94)
53. Müller L, Kirschstein T, Köhling R, Kuhla A, Teipel S (2021) Neuronal Hyperexcitability in APP SWE/PS1dE9 Mouse Models of Alzheimer's Disease. *J Alzheimers Dis Preprint*:1–15
54. Tan Y-X, Liu G-C, Chen H-L, Lu M-N, Chen B, Hu T, Zhang L, Mao R, Li S, Mei R et al (2020) Exercise-Induced Cognitive Improvement Is Associated with Sodium Channel-Mediated Excitability in APP/PS1 Mice. *Neural Plast* 2020:9132720
55. Yan S, Li Z, Li H, Arancio O, Zhang W (2014) Notoginsenoside R1 increases neuronal excitability and ameliorates synaptic and memory dysfunction following amyloid elevation. *Sci Rep* 4(1):6352
56. Kiskinis E, Kralj JM, Zou P, Weinstein EN, Zhang H, Tsioras K, Wiskow O, Ortega JA, Eggan K, Cohen AE (2018) All-Optical Electrophysiology for High-Throughput Functional Characterization of a Human iPSC-Derived Motor Neuron Model of ALS. *Stem Cell Reports* 10(6):1991–2004
57. Bando Y, Sakamoto M, Kim S, Ayzenshtat I, Yuste R (2019) Comparative evaluation of genetically encoded voltage indicators. *Cell reports* 26(3):802–813. e804

58. Grubb MS, Burrone J (2010) Activity-dependent relocation of the axon initial segment fine-tunes neuronal excitability. *Nature* 465(7301):1070–1074
59. Kole MHP, Stuart GJ (2008) Is action potential threshold lowest in the axon? *Nat Neurosci* 11(11):1253–1255
60. Hu W, Tian C, Li T, Yang M, Hou H, Shu Y (2009) Distinct contributions of Nav1.6 and Nav1.2 in action potential initiation and backpropagation. *Nat Neurosci* 12(8):996–1002
61. Wang X, Zhang X-G, Zhou T-T, Li N, Jang C-Y, Xiao Z-C, Ma Q-H, Li S: **Elevated Neuronal Excitability Due to Modulation of the Voltage-Gated Sodium Channel Nav1.6 by A β 1–42**. In: *Frontiers in neuroscience*. vol. 10 (2016) 94
62. Hoxha E, Boda E, Montarolo F, Parolisi R, Tempia F (2012) Excitability and synaptic alterations in the cerebellum of APP/PS1 mice. *PloS one* 7(4):e34726
63. Hu T, Xiao Z, Mao R, Chen B, Lu M-N, Tong J, Mei R, Li S-S, Xiao Z-C, Zhang L-F (2017) Nav β 2 knockdown improves cognition in APP/PS1 mice by partially inhibiting seizures and APP amyloid processing. *Oncotarget* 8(59):99284
64. Ren S-c, Chen P-z, Jiang H-h, Mi Z, Xu F, Hu B, Zhang J (2014) Zhu Z-r: **Persistent sodium currents contribute to A β 1-42-induced hyperexcitation of hippocampal CA1 pyramidal neurons**. *Neurosci Lett* 580:62–67
65. Good TA, Murphy RM: **Effect of β -amyloid block of the fast-inactivating K⁺ channel on intracellular Ca²⁺ and excitability in a modeled neuron**. *Proceedings of the National Academy of Sciences* 1996, **93**(26):15130–15135.
66. Kerrigan TL, Atkinson L, Peers C, Pearson HA (2008) Modulation of 'A'-type K⁺ current by rodent and human forms of amyloid β protein. *NeuroReport* 19(8):839–843
67. Chen C (2005) β -Amyloid increases dendritic Ca²⁺ influx by inhibiting the A-type K⁺ current in hippocampal CA1 pyramidal neurons. *Biochem Biophys Res Commun* 338(4):1913–1919
68. Feng B, Zhu Y, La J-H, Wills ZP, Gebhart GF (2015) Experimental and computational evidence for an essential role of Nav1.6 in spike initiation at stretch-sensitive colorectal afferent endings. *J Neurophysiol* 113(7):2618–2634
69. Lorincz A, Nusser Z (2008) Cell-type-dependent molecular composition of the axon initial segment. *J Neurosci* 28(53):14329–14340
70. Baranauskas G, David Y, Fleidervish IA: **Spatial mismatch between the Na⁺ flux and spike initiation in axon initial segment**. *Proceedings of the National Academy of Sciences* 2013, **110**(10):4051–4056.
71. Scarmeas N, Honig LS, Choi H, Cantero J, Brandt J, Blacker D, Albert M, Amatniek JC, Marder K, Bell K (2009) Seizures in Alzheimer disease: who, when, and how common? *Arch Neurol* 66(8):992–997
72. Born HA, Kim J-Y, Savjani RR, Das P, Dabaghian YA, Guo Q, Yoo JW, Schuler DR, Cirrito JR, Zheng H (2014) Genetic suppression of transgenic APP rescues Hypersynchronous network activity in a mouse model of Alzheimer's disease. *J Neurosci* 34(11):3826–3840

73. Vossel KA, Tartaglia MC, Nygaard HB, Zeman AZ, Miller BL (2017) Epileptic activity in Alzheimer's disease: causes and clinical relevance. *Lancet Neurol* 16(4):311–322
74. Gourmaud S, Shou H, Irwin DJ, Sansalone K, Jacobs LM, Lucas TH, Marsh ED, Davis KA, Jensen FE, Talos DM (2020) Alzheimer-like amyloid and tau alterations associated with cognitive deficit in temporal lobe epilepsy. *Brain* 143(1):191–209
75. Amatniek JC, Hauser WA, DelCastillo-Castaneda C, Jacobs DM, Marder K, Bell K, Albert M, Brandt J, Stern Y (2006) Incidence and predictors of seizures in patients with Alzheimer's disease. *Epilepsia* 47(5):867–872
76. Seizures (2013) **and** Epileptiform Activity in the Early Stages of Alzheimer Disease. *Jama Neurology* 70(9):1158–1166
77. Tovar KR, Bridges DC, Wu B, Randall C, Audouard M, Jang J, Hansma PK, Kosik KS (2018) Action potential propagation recorded from single axonal arbors using multielectrode arrays. *J Neurophysiol* 120(1):306–320
78. Viswam V, Obien MEJ, Franke F, Frey U, Hierlemann A: **Optimal Electrode Size for Multi-Scale Extracellular-Potential Recording From Neuronal Assemblies.** *Frontiers in Neuroscience* 2019, 13(385)
79. Bakkum DJ, Obien MEJ, Radivojevic M, Jäckel D, Frey U, Takahashi H, Hierlemann A (2019) The Axon Initial Segment is the Dominant Contributor to the Neuron's Extracellular Electrical Potential Landscape. *Advanced Biosystems* 3(2):1800308
80. Kwon T, Sakamoto M, Peterka DS, Yuste R (2017) Attenuation of Synaptic Potentials in Dendritic Spines. *Cell Reports* 20(5):1100
81. Cartailier J, Kwon T, Yuste R, Holcman D (2018) Deconvolution of voltage sensor time series and electro-diffusion modeling reveal the role of spine geometry in controlling synaptic strength. *Neuron* 97(5):1126–1136. e1110
82. Adam Y, Kim JJ, Lou S, Zhao Y, Xie ME, Brinks D, Wu H, Mostajo-Radji MA, Kheifets S, Parot V (2019) Voltage imaging and optogenetics reveal behaviour-dependent changes in hippocampal dynamics. *Nature* 569(7756):413–417
83. Yang J, Xiao Y, Li L, He Q, Li M, Shu Y (2019) Biophysical Properties of Somatic and Axonal Voltage-Gated Sodium Channels in Midbrain Dopaminergic Neurons. *Front Cell Neurosci* 13:317

Figures

Fig. 1

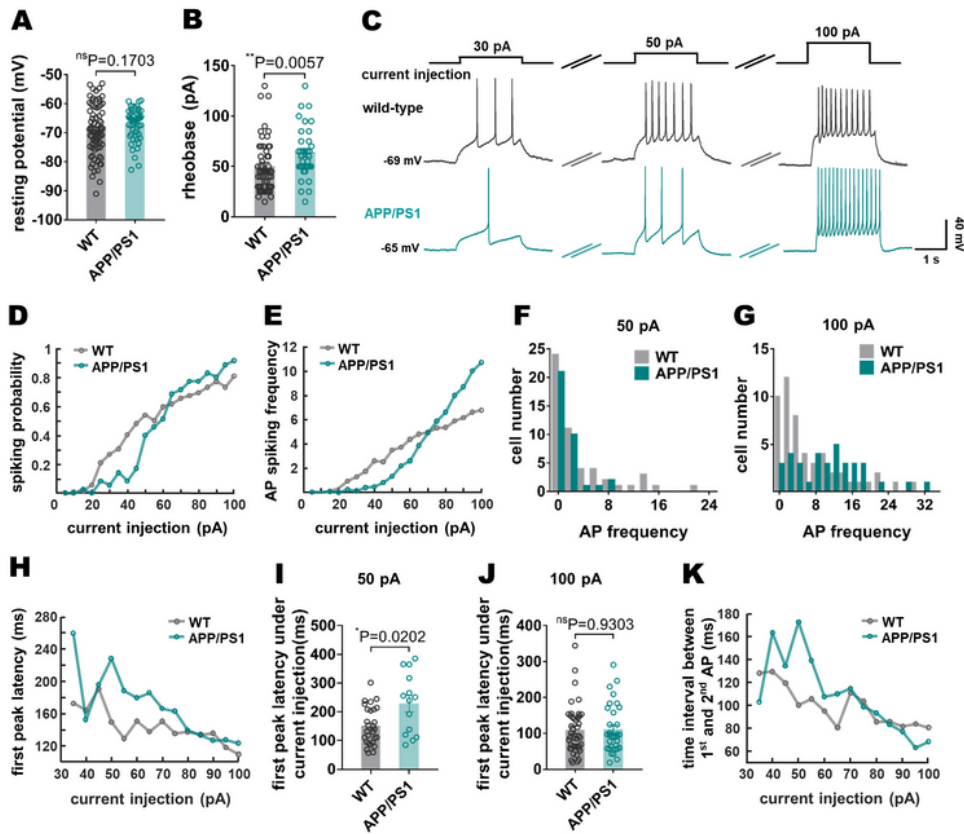


Figure 1

Intrinsic excitability increased more sharply with the simulation strength elevation in APP/PS1 mouse hippocampal neurons. A No significant difference was observed in resting potential between wild-type mice neurons (showed in gray, -69.1 ± 0.98 mV, $n = 77$) and APP/PS1 neurons (showed in teal blue, -67.1 ± 0.82 mV, $n = 48$, nsP value = 0.1703). B The APP/PS1 neurons had significantly higher rheobase under stepwise depolarizing current injection (from 5 pA to 100 pA with a 5 pA step size, and the current

injection duration and the followed rest-time duration were all about 500 ms) than wild-type neurons (APP/PS1: 63.6 ± 4.3 pA, $n = 35$; wild-type: 50.2 ± 3.7 pA, $n = 52$, **P value = 0.0057). C Typical membrane potential traces responding to stepwise current injection from 5 pA to 100 pA (the identical stimulation in Fig. 1B, here the results of 30 pA, 50 pA, and 100 pA were highlighted). D The firing probability of APP/PS1 neurons (if the neurons burst at least one AP during the current injection or not, $n = 35$) increased in the current injection pattern described in Fig. 1B when the injected current was more than 40 pA and surpassed the wild-type neurons ($n = 52$) when the current was more than 65 pA. E The firing frequency of wild-type neurons and APP/PS1 neurons in the same test of Fig. 1C. The firing frequency of APP/PS1 neurons surpassed the wild-type neurons when the current was more than 70 pA. F The distribution of wild-type and APP/PS1 neurons firing frequency when neurons are under 50 pA, 496 ms current injection (corresponding to Fig. 1E). G The distribution of wild-type and APP/PS1 neurons firing frequency when neurons are under 100 pA, 496 ms current injection (corresponding to Fig. 1E). H The first peak latency of the wild-type neurons (data of each point at least from 16 neurons) and APP/PS1 neurons (data of each point at least from 3 neurons) to the current injection pattern described in Fig. 2B. The first peak latency of the APP/PS1 neurons decreased when the current strength increased. The neurons in this figure. fired at least one AP in all current injections when the current was more than 35 pA. I The first peak latency of APP/PS1 neurons under 50 pA, 496 ms current injection was significantly longer than wild-type neurons (APP/PS1: 228.1 ± 28.2 ms, $n = 14$; wild-type: 149.6 ± 12.4 ms, $n = 28$, *P-value = 0.0202), corresponding to Fig. 1H. J No significant difference were observed between the first peak latency of APP/PS1 neurons (111.3 ± 12.0 ms, $n = 32$) and wild-type neurons ($n = 42$, 109.9 ± 10.6 ms) under 100 pA, 496 ms current injection, (APP/PS1: 111.3 ± 12.0 ms, $n = 32$; wild-type: 109.9 ± 10.6 ms, $n = 42$, nsP-value = 0.9303), corresponding to Fig. 1H. K The interval between the first peak and second time of the wild-type neurons (data of each point at least from 10 neurons) and APP/PS1 neurons (data of each point at least from one neuron) to the current injection pattern described in Fig. 1C. The neurons included in this figure fired at least two APs in all current injections when the current was more than 35 pA. Data were presented as mean \pm S.E.M.. Statistical analysis was performed using Mann-Whitney test in Fig. 1A, B, F, and G, or by unpaired t-test in Fig. 1I and J. The data acquisition rate is 21159 Hz.

Fig. 2

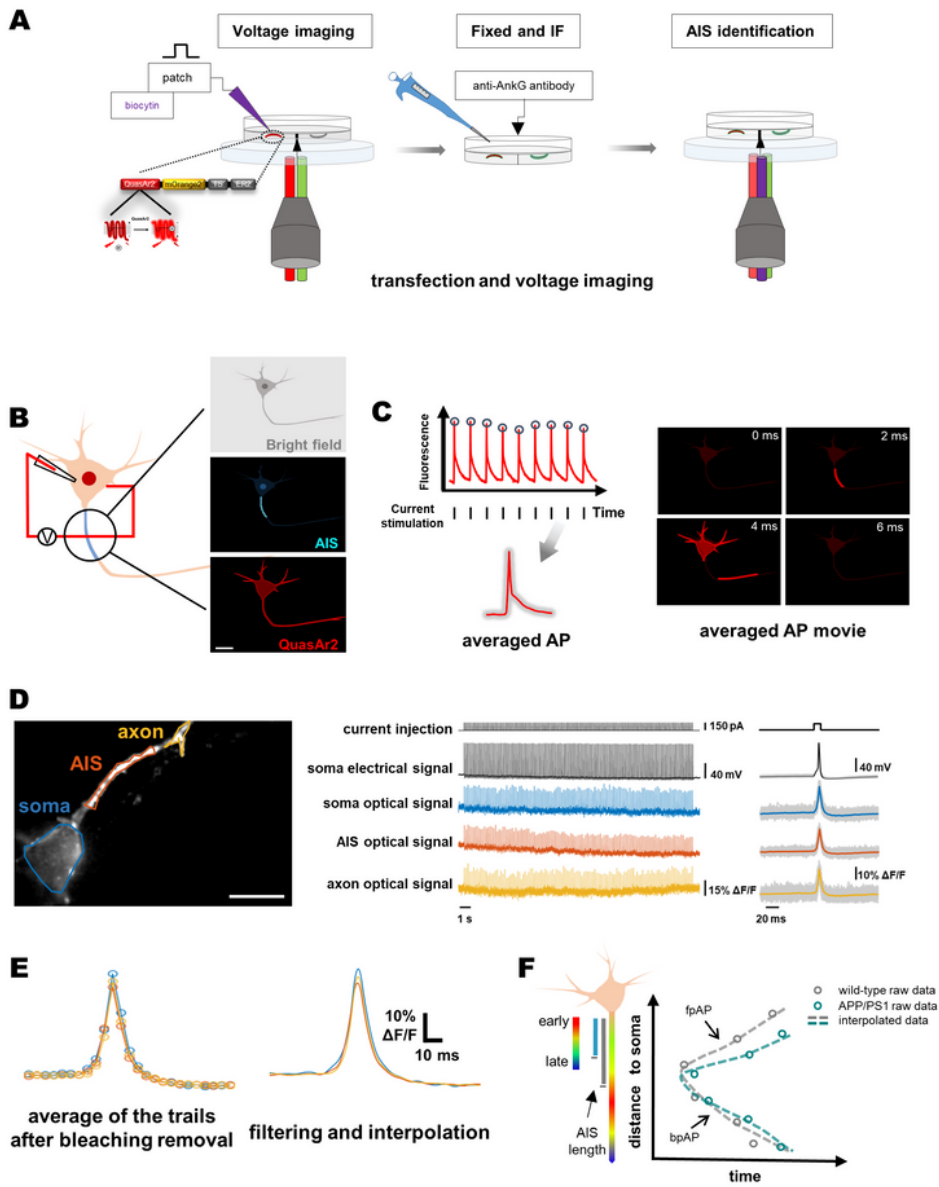


Figure 2

AP initiation and propagation in the AIS could be well-resolved via voltage imaging A The pipeline of investigating AP details in the AIS and adjacent soma, axon, and dendrites via voltage imaging. Firstly, current injection and synchronized voltage imaging were performed on cultured wild-type (control) and APP/PS1 mouse hippocampal neurons (DIV12) expressing QuasAr2-mOrange2, and biocytin was filled in the internal solution of the patch pipettes to identify the tested neurons. Then, standard IF was performed

on the neurons. After the IF, tested neurons and their AIS would be indicated via dye-conjugated streptavidin and AnkG antibody, respectively. Finally, the tested neurons and their AIS could be recognized under a microscope. A group of representative fluorescence images is shown in Supplementary Fig. 2. B A cartoon illustrating AIS identification in a neuron after voltage imaging under a microscope. C The Spike-triggered average movie was generated for the average AP waveform of each pixel in the field of view for the following interpolation. D Left, a selected cell expressing QuasAr2-mOrange2 is with current injection on the soma for the action potentials train, and different regions of interest (ROI) in the neuron in the field-of-view were polygonally outlined in different colors, corresponding to the traces in the middle column; Middle, the signals of somatic recorded electrophysiological data and corresponding voltage imaging data to the selected cell. The injected current (200 pA 10ms, 4 Hz, shown in the gray line) evoked action potential trains (electrical signal in soma, gray). The corresponding optical voltage signals were simultaneously recorded with an sCMOS camera in good synchronization (blue: soma; orange: AIS; yellow: axon). Sub-threshold electrical event (failed APs) would be well-removed in the traces; Right, the averaged electrical AP trace (black line on the top) and optical traces of the averaged AP signals (blue: soma; orange: AIS; yellow: axon) evoked by the somatic stimulation (black line on the bottom). The average traces were superimposed with single AP trails (gray lines backward). E Left, superimposed average signals of the three ROIs in Fig. 2D acquired in 484 Hz. The circle markers on the solid lines indicate the raw optical data points; Right, the corresponding 1000-times upsampled optical signal via a maximum correction-based waveform filter and cubic spline-based interpolation algorithm (interval = 2.0658 μ s) (Supplementary Fig. 3 and METHOD). F According to the high spatial-temporal AP initiation and propagation mapping from voltage imaging and interpolation, the AIS parameters (like length, distance to soma, and width, left column) and AP propagation details (AP initiation site, bidirectional propagation velocities in the AIS, soma, axon, and neighbor dendrites, right column) and diversities between the neurons from different types of the mouse like the wild-type mouse (in gray) and the APP/PS1 mouse (in teal blue) could be resolved. The circles in the right figure represent the AP arrival timing calculated from the original voltage imaging movie. The dash lines represent the AP arrival timing from the interpolated data.

Fig. 3

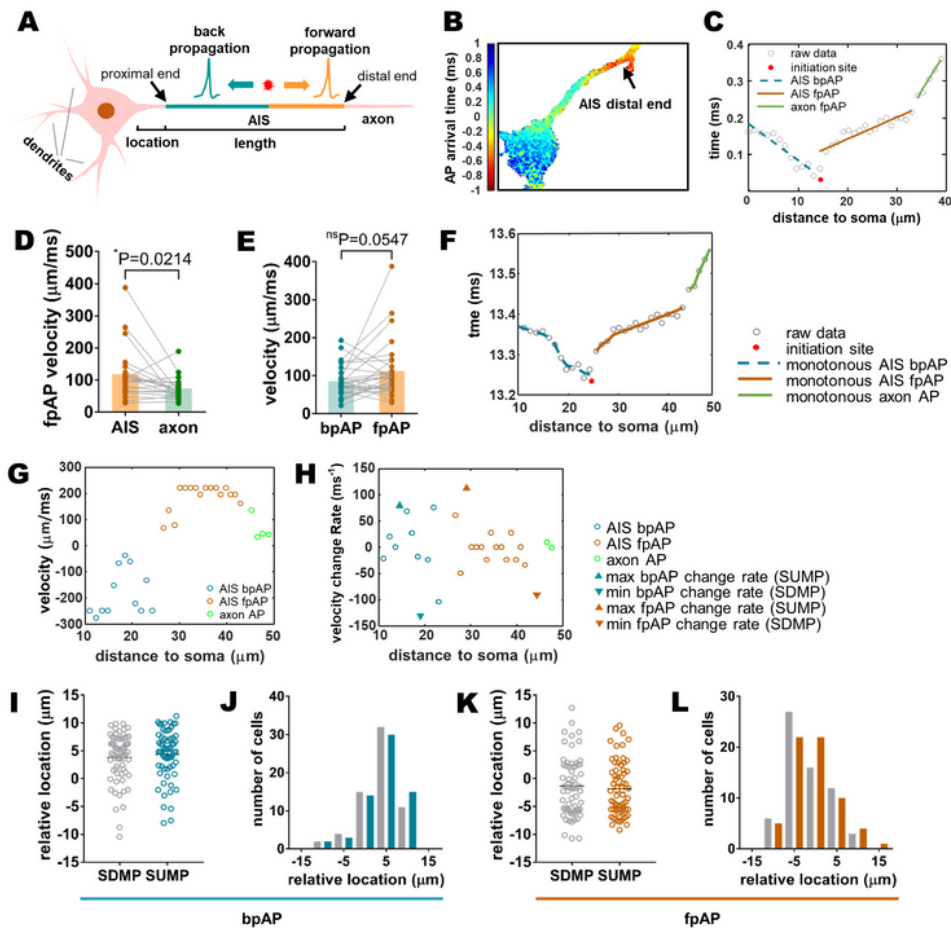


Figure 3

AP velocities were varied during propagation A Schematic diagram of a neuron, including dendrites, soma, AIS, and axon. AIS location is defined as the distance from the soma to the AIS proximal end. AIS length is defined as the distance from the proximal end to the distal end. AP is initiated in the initiation site (red star) and propagates backward (blue) and forward (orange). B The heatmap of action potential arrival timing generated from the spike-triggered average AP movie after filtering and interpolation (Fig. 2

D and E). The black arrow indicates the location where AP is initiated. C Gray circles are the AP peak arrival time at each location in the axon. The red dot is the AP initiation site. The dotted line shows mean bpAP propagation. The solid lines show mean fpAP propagation. The blue and brown lines show mean AP propagation in AIS. The green line shows AP propagation in the axon. D Paired comparison of fpAP velocities in the AIS and axon (number of pairs = 21, mean velocity in the AIS = 119.5 ± 18.64 $\mu\text{m}/\text{ms}$, mean velocity in the axon = 73.45 ± 7.76 $\mu\text{m}/\text{ms}$, *P-value = 0.0214). E Paired comparison of bpAP and fpAP velocities in the AIS (number of pairs = 29, mean bpAP velocity = 84.99 ± 7.6 $\mu\text{m}/\text{ms}$, mean fpAP velocity = 112.6 ± 14.2 $\mu\text{m}/\text{ms}$, *P-value = 0.0547). F Gray circles are the raw data of peak time. Lines are fitted by raw data using the least-squares curve fitting with linear constraints (The details of data analysis are described in METHODS). The dotted curve is bpAP propagation. The solid curves are fpAP propagation. The blue and brown curves are AP propagation in AIS. The green curve is AP propagation in the axon. The red dot is the initiation site. G Each dot is the instantaneous velocity on each location on the axon. The blue, brown, and green dots are the velocity of bpAP in the AIS, fpAP in the AIS, and fpAP in the axon. H Each dot is the instantaneous rate of a velocity change on each location in the axon. The blue, brown, and green dots are the velocity change rate of bpAP in the AIS, fpAP in the AIS, and fpAP in the axon. The blue triangle indicates the largest velocity change rate of bpAP, indicating that velocity becomes faster on this location. The blue inverted triangle shows the lowest velocity change rate of bpAP, indicating that velocity becomes slower on this location. The brown triangle and inverted triangle indicate the highest and lowest velocity change rate of fpAP. I Relative location of SDMP and SUMP of bpAP to AIS proximal end in the control group (positive: the points are in AIS, negative: the points are in hillock). Gray circle, the relative location of SDMP of bpAP (Mean \pm SEM 3.816 ± 0.5569 , n=64); blue circle, the relative location of SUMP of bpAP (Mean \pm SEM 4.333 ± 0.5581 , n=64). J Histogram of Fig. 3I. K Relative location of SDMP and SUMP of fpAP to AIS distal end in the control group (positive: the points are in the axon, negative: the points are in AIS). Gray circle, the relative location of SDPM of fpAP (Mean \pm SEM -1.814 ± 0.6093 , n=64); brown circle, the relative location of SUMP of fpAP (Mean \pm SEM -1.33 ± 0.6614 , n=64). L Histogram of Fig. 3K.

Fig. 4

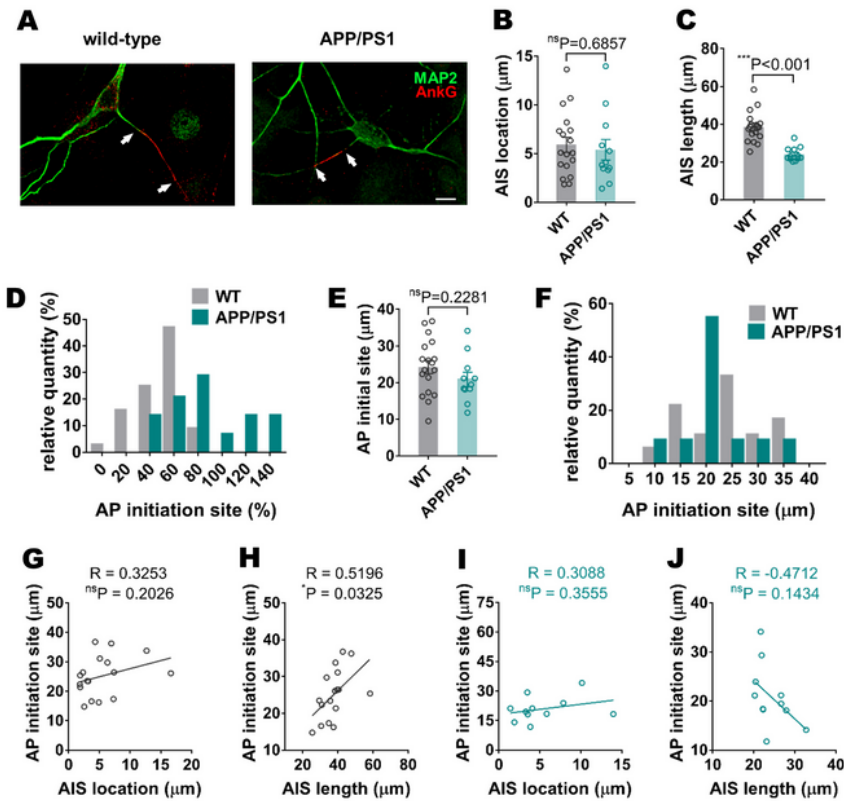


Figure 4

AP initiation site were more distal to soma in APP/PS1 mouse neurons A Immunofluorescence imaging of hippocampal neurons shows the APP/PS1 neuron has shorter AIS. MAP2 (green) denote the cell body, axon and dendrites; AnkG (red) denote the AIS, scale bars: 20 μm) B and C No significant difference was observed between the AIS location of WT neurons ($5.904 \pm 0.77 \mu\text{m}$) and APP/PS1 neurons ($5.383 \pm 1.053 \mu\text{m}$), but the AIS length of APP/PS1 neurons ($24.07 \pm 1.07 \mu\text{m}$) is significantly shorter than WT

neurons ($38.49 \pm 1.86 \mu\text{m}$). Neuron numbers: wild-type $n = 18$, APP/PS1 $n = 12$; For AIS location comparison, nsP value = 0.6857; For AIS length comparison, ***P value < 0.001 . All data were acquired from the neurons after voltage imaging. D Histogram of relative action potential initiation site in the AIS. Wild-type hippocampal neurons (gray), mean = $48.06\% \pm 3.28\%$, $n = 32$; APP/PS1 hippocampal neurons (blue), mean = $81.86\% \pm 9.12\%$, $n = 14$. E The absolute location (distance to the soma) was similar in both wild-type ($24.26 \pm 1.78 \mu\text{m}$, $n = 18$) and APP/PS1 neurons. ($20.89 \pm 1.92 \mu\text{m/ms}$, $n = 11$), nsP value = 0.2281. F Histogram of absolute AP initiation site in the AIS. Wild-type hippocampal neurons (gray), mean = $24.26 \pm 1.78 \mu\text{m}$, $n = 18$; APP/PS1 hippocampal neurons (blue), mean = $20.89 \pm 1.92 \mu\text{m/ms}$, $n = 11$. G Correlation of AIS location and absolute AP initiation site in wild-type neuron ($n = 17$, $r = 0.325$, nsP value = 0.2026). H Correlation of AIS length and absolute AP initiation site in wild-type neuron ($n = 17$, $r = 0.520$, *P value = 0.0325). I Correlation of AIS location and absolute AP initiation site in APP/PS1 neuron ($n = 11$, $r = 0.309$, nsP value = 0.3555). J Correlation of AIS length and absolute AP initiation site in APP/PS1 neuron ($n = 11$, $r = -0.471$, nsP value = 0.1434). Somatic AIS counted for most of the AIS recorded; thus only somatic AIS data were included in this study. Error bars represented S.E.M., the two-tailed unpaired t-test was employed in B and C, and the linear regression was employed in G-J.

Fig. 5

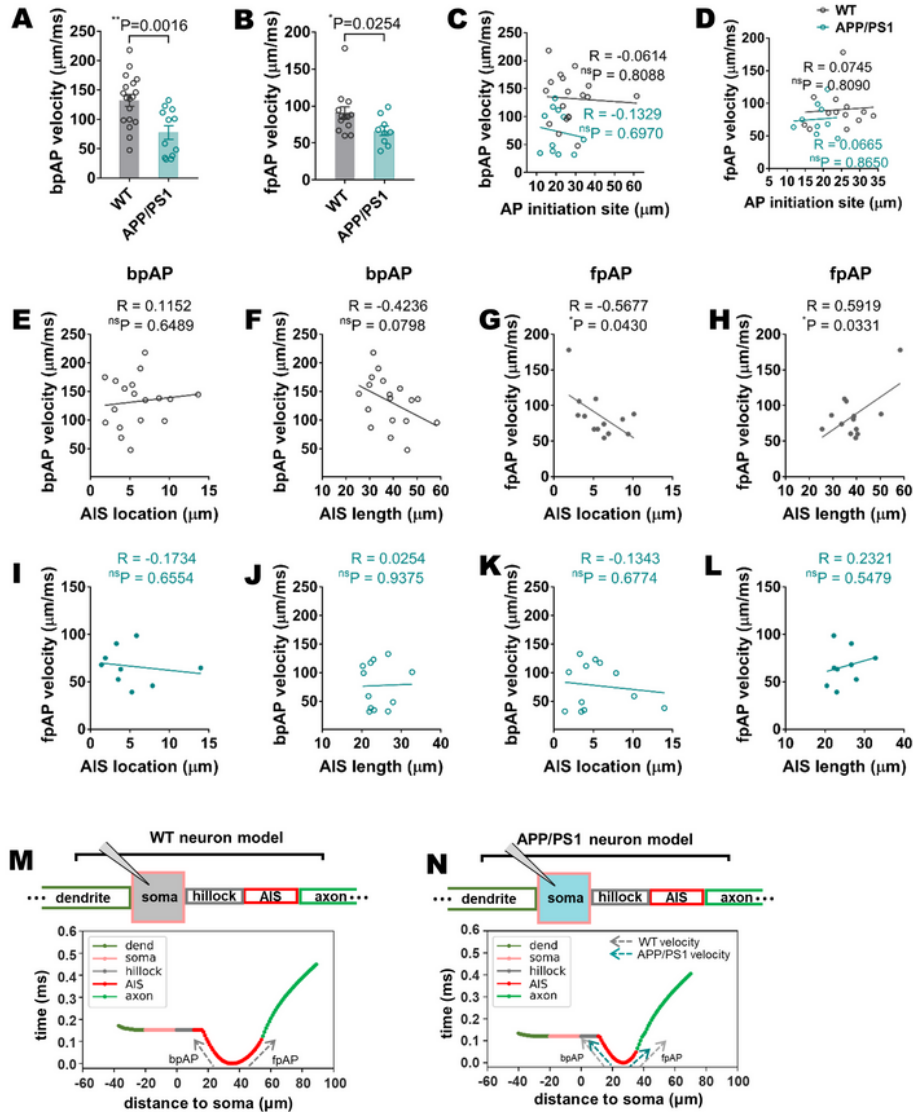


Figure 5

The neurons from APP/PS1 mice had lower bpAP and fpAP velocities than neurons from wild-type mice. We compared the bpAP and fpAP velocities in neurons from APP/PS1 mice and wild-type mice. Our data showed that compared to wild-type neurons, both bpAP and fpAP velocities in APP/PS1 neurons were lower. Moreover, our data suggested that the fpAP velocity negatively correlated with AIS location and positively correlated with AIS length. A The bpAP velocities in the AIS in APP/PS1 neurons (77.49 ± 11.55

$\mu\text{m}/\text{ms}$, $n = 12$) were significantly lower than WT neurons ($132.5 \pm 10.33 \mu\text{m}/\text{ms}$, $n = 18$). **P-value = 0.0016. B The fpAP velocities in the AIS in APP/PS1 neurons ($66.42 \pm 6.51 \mu\text{m}/\text{ms}$, $n = 9$) were significantly lower than WT neurons ($90.42 \pm 8.446 \mu\text{m}/\text{ms}$, $n = 13$). *P-value = 0.0254. C Correlation of bpAP velocity and absolute AP initiation site in wild-type neuron ($n = 18$, $r = -0.061$, nsP value = 0.8088) and APP/PS1 neuron ($n = 11$, $r = -0.133$, nsP-value = 0.6970). D Correlation of fpAP velocity and absolute AP initiation site in wild-type neuron ($n = 13$, $r = 0.075$, nsP value = 0.8090) and APP/PS1 neuron ($n = 9$, $r = -0.067$, nsP-value = 0.8650). E Correlation of AIS location and bpAP velocity in wild-type neuron ($n = 18$, $r = 0.115$, nsP-value = 0.6489). F Correlation of AIS length and bpAP velocity in wild-type neuron ($n = 18$, $r = -0.424$, nsP-value = 0.0798). G Correlation of AIS location and fpAP velocity in wild-type neuron ($n = 13$, $r = -0.568$, *P-value = 0.0430). H Correlation of AIS length and fpAP velocity in wild-type neuron ($n = 13$, $r = 0.592$, *P-value = 0.0331). I Correlation of AIS location and bpAP velocity in APP/PS1 neuron ($n = 12$, $r = -0.134$, nsP-value = 0.6774). J Correlation of AIS length and bpAP velocity in APP/PS1 neuron ($n = 12$, $r = 0.025$, nsP-value = 0.9375). K Correlation of AIS location and fpAP velocity in APP/PS1 neuron ($n = 9$, $r = -0.173$, nsP-value = 0.6554). L Correlation of AIS length and fpAP velocity in APP/PS1 neuron ($n = 9$, $r = 0.232$, nsP-value = 0.5479). M Wild-type neuron model. Upper, the schematic diagram of a somatic multi-compartment model, depicting all the model compartments and the injected stimulus in the simulation. Soma compartment was attached to a dendrite compartment and a hillock compartment. AIS compartment was attached to a hillock compartment, then attached to an axon compartment. The model parameters are shown in Supplementary Table S2. The stimulus was a 1 nA current that lasted for 1 ms. The current stimulus was injected into the center of the soma. Lower, the arrival time of action potential peaks on some segments. The black line labeled these segments in the upper schematic diagram. Different compartments are shown in different colors. The slopes of dotted arrows are the mean bpAP and fpAP velocities in the AIS compartment. N APP/PS1 neuron model. Upper, the schematic diagram of a somatic multi-compartment model, depicting all the model compartments and the injected stimulus in the simulation. The compartments and stimulus were the same with wild-type neurons. The only three differences are: 1) shorter AIS, 2) lower sodium channel density in the AIS, 3) higher sodium density in the axon. The model parameters are shown in Supplementary Table S2. Lower, the arrival time of action potential peaks on selected segments. The black line labeled these segments in the upper schematic diagram. Different compartments are shown in different colors. The slopes of dotted red (pink) arrows are the mean bpAP and fpAP velocities in the AIS compartment in the wild-type (APP/PS1) neuron model. Error bars represented S.E.M., the two-tailed unpaired t-test was employed in A and B, and the linear regression was employed in C-L.

Fig. 6

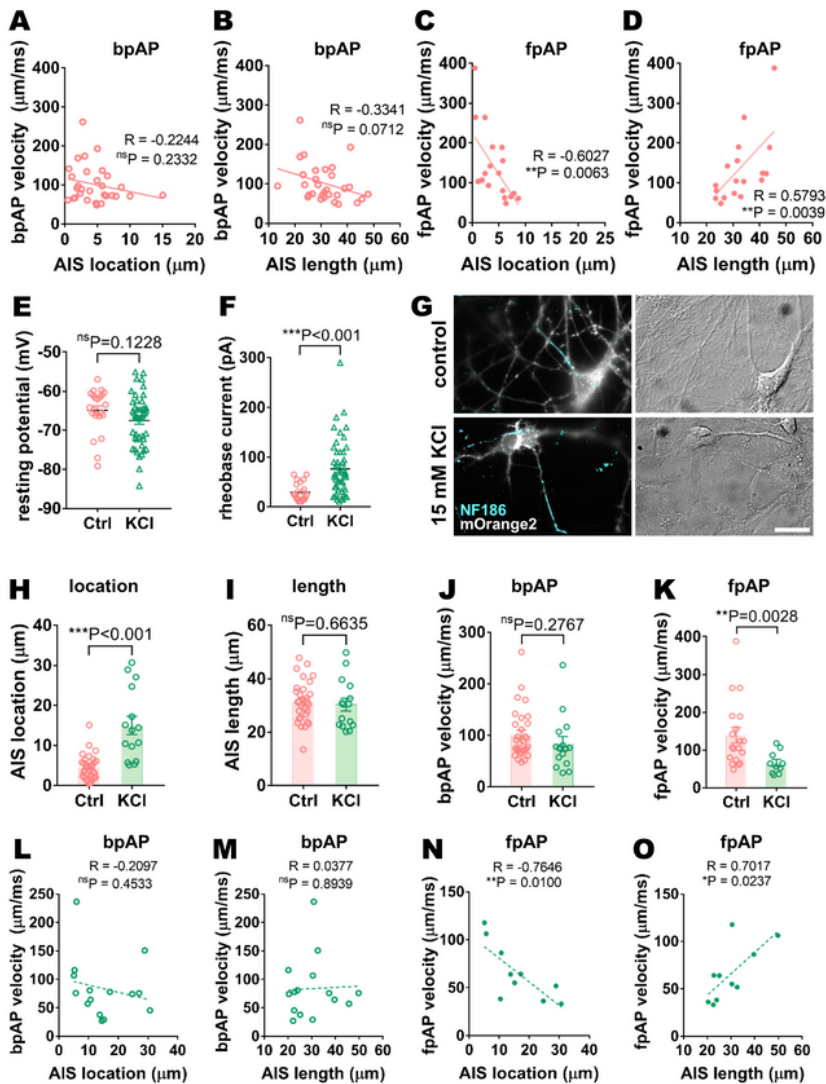


Figure 6

The fpAP velocity was negatively correlated with AIS location and positively correlated with AIS length. A Correlation of AIS location and bpAP velocity ($n = 30$, $r = -0.224$, nsP -value = 0.2332). B Correlation of AIS length and bpAP velocity ($n = 30$, $r = -0.334$, nsP -value = 0.0712). C Correlation of AIS location and fpAP velocity ($n = 19$, $r = -0.603$, $**P$ -value = 0.0063). D Correlation of AIS length and fpAP velocity ($n = 19$, $r = 0.579$, $**P$ -value = 0.0093). E No significant difference was observed in the resting potential of neurons in

the control group (-64.9 ± 1.2 mV, $n = 22$) and chronic KCl treatment group (-67.5 ± 0.97 mV, $n = 46$), nsP-value = 0.1228 F 48 hours 15 mM KCl treatment significantly increases the rheobase current (76.18 ± 7.718 pA, $n = 46$) of the neurons compared to the control group neurons (29.55 ± 3.877 pA, $n = 22$), ***P-value < 0.001. G Representative images of cultured WT rat hippocampal neurons (DIV12) without treatment (as control, upper) and with 48 hours 15 mM KCl treatment (lower). All the neurons were transfected in DIV7 with QuasAr2-mOrange2 plasmid. (Left) Selected neurons (white) and their AISs (blue) were indicated by the fluorescence of mOrange2 and axonal marker NF186, respectively; (Right) The corresponding DIC images to the neurons in the left column (Scale bars: 20 μ m). H AIS location (AIS distance to the soma) comparison. AIS is significantly far from soma in 48 hours 15 mM KCl treatment group (14.98 ± 2.30 μ m, $n = 15$) than in control group (6.76 ± 0.85 μ m, $n = 45$), ***P-value < 0.001. I No significant difference was observed between the AIS length of the control group (32.51 ± 1.16 μ m, $n = 45$) and 48 hours 15 mM KCl treatment group (30.26 ± 2.40 μ m, $n = 15$), nsP-value = 0.6635. J No significant difference was observed in the bpAP velocities in the AIS in control group neurons (101.3 ± 8.861 μ m/ms, $n = 30$) and 48 hours 15 mM KCl treatment group neurons (83.74 ± 13.89 μ m/ms, $n = 15$), nsP-value = 0.2767. K fpAP velocities in the AIS in 15 mM KCl treatment group neurons (65.33 ± 9.30 μ m/ms, $n = 10$) are lower than control groups (138.8 ± 20.1 μ m/ms, $n = 19$), **P-value = 0.0028. L-O Correlation between the bpAP/fpAP velocities and AIS location/length: (L) Correlation between bpAP velocity and AIS location ($n = 15$, $r = -0.210$, nsP-value = 0.4533); (M) Correlation between bpAP velocity and AIS length ($n = 15$, $r = 0.038$, nsP-value = 0.8939); (N) Correlation between fpAP velocity and AIS location ($n = 10$, $r = -0.765$ **P-value = 0.01); (O) Correlation between fpAP velocity and AIS length ($n = 10$, $r = 0.702$ *P-value = 0.0237). Error bars represented S.E.M., the two-tailed unpaired t-test was employed in E-F and H-K, and the linear regression was employed in A-D and L-O.

Fig. 7

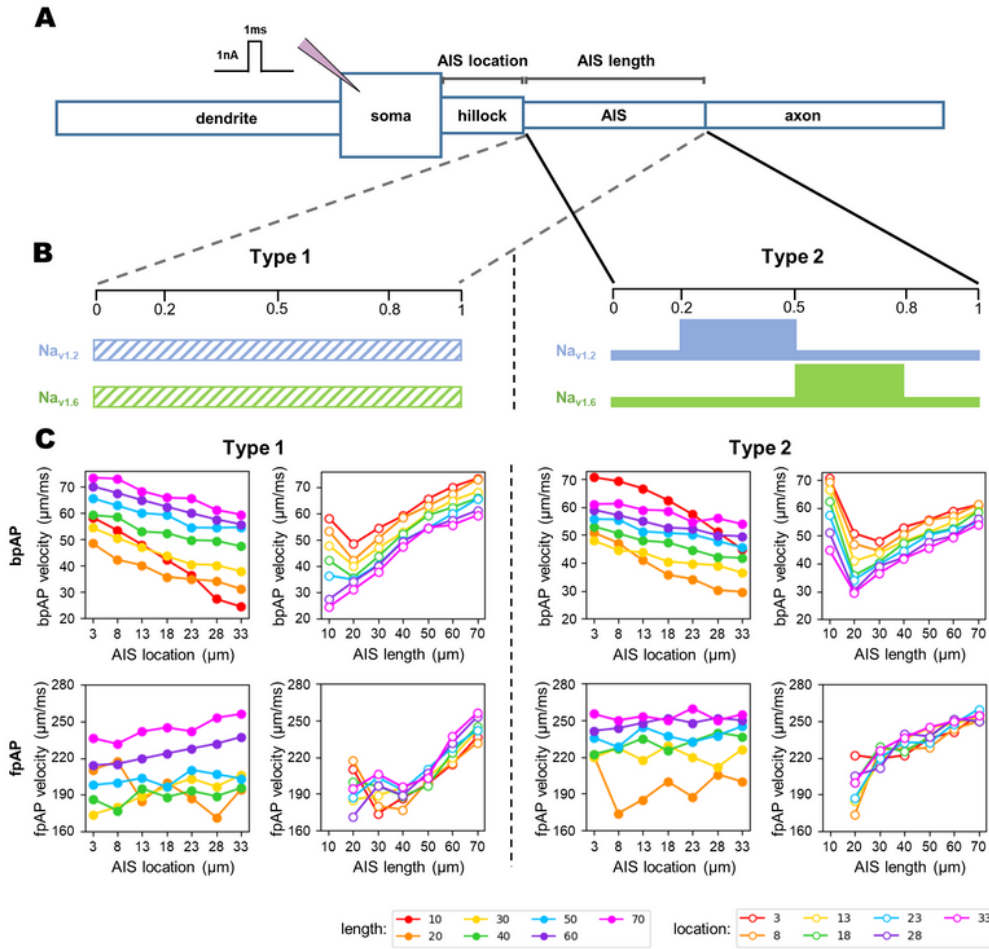


Figure 7

Simulations with two types of sodium ion channel distribution A Schematic diagram of the multi-compartment model, depicting all the neuronal compartments and the injected stimulus in the simulation. Soma was attached to a dendrite and an axon. The axon included a hillock, an AIS, and an axon. The stimulus was a 1 nA current that lasted for 1 ms. The current stimulus was injected into the center of the soma. B Left, Type 1 sodium channels distribution in the AIS. The height of the bar represents the density

of ion channels. The blue and green bars represented distributions of Nav1.2 and Nav1.6 channel densities, respectively. The density of AIS ion channels was uniform along with the AIS in Type 1. Right, Type 2 sodium channels distribution in the AIS. The densities of Nav1.2 and Nav1.6 were high on proximal (20%-50% of full length) and distal (50%-80% of full length) AIS. Type 2 was a non-uniform distribution. C The interaction between bpAP (upper row) / fpAP (lower row) velocities and AIS location (left column) / length (right column) upon adjusting AIS length (solid dots) and location (circles). The left and right parts were the results when sodium channel distributions were set as Type 1 and Type 2. (When AIS length is short, e.g., 10 μm , action potentials are initiated in the axon or the end of distal AIS. Therefore, the fpAP velocity is meaningless. Thus, we did not record the fpAP velocity when the AIS length was 10 μm .)

Supplementary Files

This is a list of supplementary files associated with this preprint. Click to download.

- [combinedS0923.pdf](#)